

A substitutional quantum defect in WS₂ discovered by high-throughput computational screening and fabricated by site-selective STM manipulation

John C. Thomas^{1,2,3*†}, Wei Chen^{4†}, Yihuang Xiong^{3†}, Bradford A. Barker⁵, Junze Zhou¹,
Weiru Chen³, Antonio Rossi^{1,2,6}, Nolan Kelly⁵, Zhuohang Yu^{7,8}, Da Zhou⁹, Shalini Kumari^{7,8},
Edward S. Barnard¹, Joshua A. Robinson^{7,8,9,10}, Mauricio Terrones^{7,8,9,10}, Adam
Schwartzberg¹, D. Frank Ogletree¹, Eli Rotenberg⁶, Marcus M. Noack¹¹, Sinéad Griffin^{1,2},
Archana Raja^{1,2}, David A. Strubbe⁵, Gian-Marco Rignanes⁴, Alexander Weber-Bargioni^{1,2*},
and Geoffroy Hautier^{3*}

¹*Molecular Foundry, Lawrence Berkeley National Laboratory, Berkeley, CA 94720, United States of America*

²*Materials Sciences Division, Lawrence Berkeley National Laboratory, Berkeley, CA, United States of America*

³*Thayer School of Engineering, Dartmouth College, Hanover, NH 03755, USA*

⁴*Institute of Condensed Matter and Nanoscience, Université catholique de Louvain, Louvain-la-Neuve 1348, Belgium*

⁵*Department of Physics, University of California, Merced, Merced, CA 95343, USA*

⁶*Advanced Light Source, Lawrence Berkeley National Laboratory, Berkeley, CA 94720, United States of America*

⁷*Department of Materials Science and Engineering, The Pennsylvania State University, University Park, PA 16802 United States of America*

⁸*Center for Two-Dimensional and Layered Materials, The Pennsylvania State University, University Park, PA, 16802 United States of America*

⁹*Department of Physics, The Pennsylvania State University, University Park, PA, 16802 United States of America*

¹⁰*Department of Chemistry, The Pennsylvania State University, University Park, PA, 16802 United States of America*

¹¹*Applied Mathematics and Computational Research Division, Lawrence Berkeley National Laboratory, Berkeley, CA 94720, United States of America*

**jthomas@lbl.gov, afweber-bargioni@lbl.gov, geoffroy.hautier@dartmouth.edu*

†These authors contributed equally.

ABSTRACT

Point defects in two-dimensional materials are of key interest for quantum information science. However, the parameter space of possible defects is immense, making the identification of high-performance quantum defects very challenging. Here, we perform high-throughput (HT) first-principles computational screening to search for promising quantum defects within WS₂, which present localized levels in the band gap that can lead to bright optical transitions in the visible or telecom regime. Our computed database spans more than 700 charged defects formed through substitution on the tungsten or sulfur site. We found that sulfur substitutions enable the most promising quantum defects. We computationally identify the neutral cobalt substitution to sulfur (Co_S⁰) and fabricate it with scanning tunneling microscopy (STM). The Co_S⁰ electronic structure measured by STM agrees with first principles and showcases an attractive quantum defect. Our work shows how HT computational screening and nanoscale synthesis routes can be combined to design promising quantum defects.

INTRODUCTION

Point defects in semiconductors are considered as building blocks for quantum information science (QIS) applications. Optically-active quantum defects (OQDs) can be used in quantum sensing, memory, and networks¹⁻⁴. The performance of an OQD depends on its fundamental properties and limitations that can vary across defects^{5,6}. Certain defects, such as the silicon-divacancy center in diamond, show robust optical coherence but low spin coherence, while the NV⁻ center in diamond shows high spin coherence but lower optical coherence^{7,8}. The identification of OQDs in a specific host with optimal spin, optical, and electronic properties is essential to the development of QIS applications.

Two-dimensional (2D) materials, particularly transition metal dichalcogenides (TMDs), provide an enormous phase space of functionality with tunable and exceptional spin, optical and electronic properties⁹⁻¹⁷. Additionally, as materials are reduced from bulk to lower dimensionality, the spin-coherence lifetime of an OQD is expected to increase¹⁸. WS₂, specifically, is a highly modifiable TMD that has been predicted to have long spin coherence times (T_2 of ~ 11 ms)^{18,19}. A decisive factor for an OQD is the appearance of in-gap localized states making it important to understand and measure the electronic levels induced by a defect in a given 2D host. While a number of techniques can routinely resolve

the atomic lattice, the electronic levels introduced by the defect in the host are not easily accessible by most experimental techniques. However, scanning tunneling microscopy (STM) and scanning tunneling spectroscopy (STS) can probe atomic-scale defects at the required length scale^{20,21}. This has been used to characterize many defects in 2D materials, e.g., carbon radical dopants, chalcogen vacancies, oxygen substitutions, and a variety of metal substitutions^{15,16,20,22–24}. Next to these experimental developments, first-principles approaches have been successfully used to compute and understand the properties of quantum defects in bulk semiconductors and 2D hosts^{25–28}. First principles techniques have even been used to suggest QDs in 2D materials, but these studies have remained targeted on a few defects and have not browsed the large elemental space of possible defects^{29–33}.

Here, we use first principles high-throughput (HT) computing to build a database of point defects in WS₂ considering all possible substitutional defects from 57 elements, aiming to accelerate the exploration of defect chemical space in WS₂³⁴. We use this database to identify a handful of promising defects and show that the substitution of cobalt on sulfur (Co_S) in WS₂ is especially appealing. First principles computations indicate that the neutral Co_S shows several localized levels in the band gap, spin multiplicity, and a potential for bright telecom emission. This defect is then synthesized *in situ*, examined with STM/STS, and the measured energy levels confirm and benchmark the theoretical predictions, which highlights an attainable two-level quantum system.

RESULTS

High-Throughput Search

A greatly sought-after electronic structure for an QD involves two localized defect levels (one occupied, the other unoccupied) well within the band gap³⁵. This requires a precise matching of defect and band edge levels. Additionally, the optical transition between these defect levels should be bright and exhibit large transition dipole moments (TDMs). While having localized defect levels within the band gap is not in itself necessary for developing QDs, this electronic structure has advantages in terms of brightness and robustness versus temperature³⁶. With the 2.4 eV electronic band gap for WS₂, finding defect levels that are at the same time isolated within the band gap and with transitions in the telecom or visible range (from 750 meV up to 2 eV) should be achievable. However, identifying defects that could act as an QD within WS₂ is challenging.

To search for such a defect, we have built a database with the computed electronic structure of 757 charged point defects in WS₂ considering either the tungsten (M_W) or sulfur (M_S) substitution site (see Fig. 1a). All the elements from the periodic table are used with the exception of rare-earths and transuranides. We start our screening by computing the relaxed structure and formation energies of the

defect in multiple charge states within Density Functional Theory (DFT) in the generalized gradient approximation (GGA). Single-particle energies and band gaps are notoriously underestimated within DFT and one of the gold standards in defect computation is to use hybrid functionals such as PBE0 which adds a fraction of Fock exchange to the GGA functional^{26,37}.

Recently, we have shown that for 2D materials, using a modified fraction of Fock exchange for the defect and the host is not adequate and we use here an approach combining a different amount of Fock exchange for defect levels and band edges (see Methods)³⁷. The use of hybrid functionals leads to a significantly higher computational cost and can preclude broad screening. Here, we accelerate the hybrid computation by fixing the wave function from DFT and applying the hybrid functional Hamiltonian from PBE0³⁸. This single-shot PBE0 approach (or PBE0₀) is similar to the single-shot *GW* (G_0W_0) approach and enables single-particle energy predictions that are much improved compared to DFT at a minimal computational overhead, which we have used for defects in silicon³⁸.

Our computational database includes formation energies, spin state, and single-particle electronic energy levels for all the possible charged defects. It also contains the TDMs between these single-particle levels indicating optical transition brightness. We use this database to search for attractive OQD candidates. Point defects in semiconductors can have different charge states depending on the Fermi level (E_F). Certain charge states are not stable for any E_F within the band gap. While we do not study how a given E_F can be achieved (e.g., through doping or gating) we only consider defects in a charge state that is stable for a range of E_F within the band gap. In addition, we focus on charged defects with possible optical transitions between defect levels localized within the band gap. No criteria on the formation energy other than the need for the charged defect to have a range of E_F in which it is stable was applied in our screening. For these defects, we evaluate their single-particle excitation energies and TDMs. Fig. 1b shows the TDM versus excitation energy for all defects. We differentiate between M_S and M_W defects as well as singlets and multiplets. Few defects show high brightness (with a TDM of at least 2.5 D) and an excitation energy within the telecom or visible range (single-particle excitation energy > 750 meV) (see Supplementary Table 1 and Supplementary Figs. 1 and 2 for a full list with their single-particle levels). We identify a series of potential singlet OQDs that could act as single-photon emitters and are formed through the substitution of W with a main group element: Sb_W^{-1} , P_W^{-1} , Pb_W^{-2} , N_W^{-1} , and C_W^{-2} . Only two transition metal defects appear as promising singlets: Os_W and Ti_S . For quantum applications, defects that possess a nonzero spin are often desirable and are called spin-photon interfaces^{4,39–41}. In WS_2 , spin multiplet defects only appear through sulfur substitution: Co_S^0 , Fe_S^0 , Zn_S^0 , Si_S^{-1} , and W_S^{+1} except for Ru_W^0 . The W_S defect has been suggested as an OQD by Tsai et al. as well, but in the zero charge state²⁹. Notably, common substitutional defects to tungsten in WS_2 : Re, V, Nb, Mo, and Cr, do not show an adequate electronic structure (see Supplementary Fig. 3)^{20,42–45}. They all have at most one level in

the band gap of the substitutional d orbital character that is slightly above the valence band edge (V) or below the conduction band (Cr and Re). They are only excitable optically through a transition between a localized defect state and a delocalized band level forming a bound exciton³⁶. Our findings agree with experimental results from photoluminescence or STS on M_W defects^{20,42,44,45}.

While substitutional transition metals on W sites are easy to synthesize^{11,46}, our screening results show that this is not the most promising approach for OQD discovery. All our candidate transition metal OQDs except Ru_W^0 and Os_W^0 show up instead as M_S . Fig. 2a shows the different electronic structure for M_W and M_S in a molecular orbital diagram picture when M is a transition metal⁴⁷. For both substitutions, the d orbitals of the defect mix with either sulfur (M_W) or tungsten (M_S) forming bonding and anti-bonding states separated by Δ_{AB} . Additionally the different d orbitals are split in three groups: (d_{xz}, d_{yz}) , $(d_{xy}, d_{y^2-x^2})$ and d_{z^2} with an energy Δd according to crystal field splitting theory. For the sake of simplicity, we assume here a C_{3v} and D_{3h} point group respectively for the M_S and M_W defects, where lower symmetry through Jahn-Teller distortions are also possible. We performed bonding analysis, and determined density of states, for all 3d transition metal defects (Supplementary Fig. 4) and we observed a smaller splitting between bonding and anti-bonding states for M_S versus M_W (Δ_{AB}). This can be rationalized by the different atomic positions for sulfur and tungsten orbitals. Additionally, the splitting between d orbitals (Δd) is higher for M_S versus M_W . Fig. 2b shows the positions of bonding and anti-bonding molecular orbitals across the 3d series (M_W (blue) and M_S (yellow) in the neutral charge state), where 3d atomic orbitals shift to lower energy from Ti to Cu. M_S substitutions show clear advantage in terms of a smaller Δ_{AB} and larger Δd , which leads to d - d transitions in the telecom or visible range and enables more potential for OQDs with two levels localized in the band gap.

Candidates

While our analysis shows that within gap d - d transitions are more likely in M_S and rationalizes why there are still differences between M_S defects. Fig. 1 shows that Co_S^0 is by far the most attractive OQD considering its non-singlet (doublet) spin multiplicity, its large excitation energy, and transition dipole moment. We compute the electronic structure and formation energy for this Co_S^0 defect within full-fledged PBE0 computations including structural relaxation and self-consistency. We plot the defect formation energy for different charge states of Co_S versus E_F in Fig. 3a. The defect is stable in its zero charge state spanning a large E_F range. The two thermodynamic charge transition levels correspond to (+/0) at 0.4 eV above the valence band maximum (VBM) and (0/−) at 0.4 eV below the conduction band minimum (CBM).

The electronic structure of the neutral Co_S^0 is shown in Fig. 3b. A full description of the electronic structure for all three charge states is given in Supplementary Fig. 5. The neutral defect undergoes a Jahn-

Teller distortion towards the C_s symmetry. While there is significant mixing with the host, the projection on the Co-3d orbitals is provided in Fig. 3b with the wavefunctions illustrated in Fig. 3c. The defect shows occupied $d_{xy} + d_{xz}$ and d_{z^2} states well within the band gap that can be excited to the unoccupied $d_{x^2-y^2}$ state below the conduction band. The lowest energy transition is between the d_{z^2} and $d_{x^2-y^2}$ states and sits at a 1.4 eV difference in single-particle energies and shows a TDM of 1.2 D. All these values are obtained from full PBE0 but confirm the prediction from our screening at the single-shot level. The zero-phonon lines (ZPL) associated with this transition are computed within the constrained-occupation DFT by imposing the electron occupation (or needed unoccupation) of the d_{z^2} and $d_{x^2-y^2}$ states and relaxing the structure. We obtain a ZPL of 0.96 eV, well within the telecom region. Transition from the lower orbital ($d_{xy} + d_{xz}$) to $d_{x^2-y^2}$ is significantly higher with a ZPL of 1.18 eV (and a TDM of 3.0 D). The first excitation with ZPL of 0.96 eV results in a ΔQ of 2.47, Huang-Rhys factor of 8.66, and overall results in a Debye-Waller factor of 0.017 %. Similar values have been reported by Li and coauthors on C_s in WS_2 (0.003%)³³. On the other hand, the second excitation of Co_S with a ZPL of 1.18 eV and a transition dipole moment 3.0 D exhibits a Debye-Waller factor of around 30%. A photonic cavity may be required to significantly enhance the zero-phonon emission^{15,48}. All these results confirm the interest of the neutral Co substitutional defect as it combines emission in the telecom and possesses doublet spin multiplicity.

Co_S Fabrication and Characterization

In order to benchmark the presented screening approach, we create and characterize the Co_S defect. Comparisons between the specific energy levels and effective orbital symmetries enable a direct comparison with the HT screening approach and first-principles computations in general. In order to fabricate the Co_S defect in WS_2 , we make use of a tailored experimental workflow inside a low temperature and ultrahigh vacuum (UHV) scanning probe microscope (SPM) that is shown in Fig. 4a-c. Sulfur vacancies (V_S) within otherwise as-grown WS_2 are created by resistively heating the sample and, in tandem, exposing it to a low incidence angle Ar^+ sputtering beam (Fig. 4a)⁴⁹. This technique produces a high density of V_S available for functionalization and subsequent reactivity. As adsorbed cobalt has been shown to be unstable on pristine TMD systems, such as MoS_2 and WS_2 , we are able to make use of adsorbed instability near the VBM of WS_2 (below -1.3 V) to systemically induce diffusion and/or evaporation events with the SPM tip^{50,51}. A Co physical vapor deposition apparatus (Fig. 4b) in UHV deposits randomly adsorbed Co to a defective $WS_2/MLG/SiC(0001)$ sample, which is held at liquid helium temperatures, at submonolayer coverage. The bias over an adsorbed Co atom can then be ramped towards the tip-induced diffusion energy range to effectively excite the Co adatom into a V_S for Co_S defect creation (see Supplementary Fig. 6 for adsorbate behavior on as-grown WS_2). Fig. 4d-g shows resulting data at each fabrication workflow

step with scanning tunneling micrographs. Linear defects are identified as one dimensional inversion domains, which are a result of the V_S creation process and has been described in detail elsewhere⁴⁹. We then focus on the realization of Co_S . STM images, taken in constant-current mode, over a single Co defect are acquired before a Co diffusion event and after Co_S formation, where the apparent height is reduced by 0.14 nm (Fig. 4h).

In order to investigate the evolved electronic structure with SPM, we make use of STS and differential conductance mapping, which are representative of the local density of states (LDOS) over a given defect. Point STS over Co_S is shown in Fig. 5a-b, where in-gap states near 0.36 eV and 0.47 eV are measured. To make a clear distinction between adsorbed Co states, V_S , as-grown WS_2 , and Co_S , point spectra are compared in Supplementary Fig. 7. We attribute peak broadening to electronic-phonon coupling, where effective electron-phonon coupling strength is estimated with a single-mode Franck-Condon model¹⁶. We include multiple phonon modes and additional quanta of each mode (available for co-excitation) in the description detailed in Supplementary Fig. 8 to explain dI/dV signal strength and broadening observed beyond the model approximation. Additionally, a resonance peak is identified at negative voltages (-0.84 ± 0.06 eV) that is attributed to electronic charging from the underlying substrate to Co_S , which shifts the defect to an anion state, where an electron is, on average, donated to available Co_S defect levels. Spatially resolved DOS below the charging onset is comparable to that of the occupied orbitals in the anionic state and to the charge neutral state above this onset. Fig. 5c-e shows high-resolution differential conductance image maps that detail electronic orbital densities measured at -0.9 eV, 0.36 eV, and 0.47 eV. The LDOS at these energies are further benchmarked against calculations at the PBE0 level of theory and shown in Fig. 5f-h for each energy range experimentally measured, where Co_S unoccupied orbitals are hybridized with bonded W atoms and are ~ 1.5 nm in diameter (see Supplementary Fig. 9 for simulated STS for charge states presented). We find strong agreement between experiment and theoretically obtained energy levels and orbital symmetries, where we can then assign the dI/dV peak at 0.36 eV to predominately $d_{x^2-y^2}$ orbital density, and the peak measured at 0.47 eV to a mixing of d_{yz} and d_{xz} orbitals at the Co_S charge neutral state. The peak at -0.84 eV is attributed to the Co_S charging (to Co_S^{-1}), and is discussed in further detail below. Quantitatively, the $d_{x^2-y^2}$ state is experimentally 0.64 eV below the CBM while theory predicts a level 0.5 eV below the CBM, indicating a good agreement.

We attribute the sharp peak at -0.84 eV to a charging process of the neutral cobalt to the anionic Co_S^{-1} state. This charging is due to the localized tip-induced band bending process has been described in the literature on similar systems^{16,52}. The Co_S lowest unoccupied state is occupied at adequate negative voltages and alters the Co_S charge state making it anionic, detailed in Fig. 5i-j. The E_F of WS_2 has been shown to be driven by the heterostructuring with graphene⁵³, where graphene is more susceptible to local doping and, here, is altered so that an electron is on average donated to the Co_S defect. The

neutral/anionic charge transition level is computed to be around 2.1 eV above the VBM (see Fig. 3) which is close to the charge transition level for V_S (see Supplementary Fig. 10) for which a charging peak at a similar position is observed for the same type of sample¹⁶. The charging peak near -0.84 eV varies spatially as the bias is ramped to more negative values: the radius of the ring around the defect center increases. In order to increase STS statistics, we perform an autonomous hyperspectral experiment over Co_S (see Supplementary Notes 1 and 2 in addition to Supplementary Figs. 11-14)²¹. The charging peak is found to energetically shift between a minimum of -0.924 eV and a maximum of -0.627 eV during point STS measurements, which amounts to a ~ 0.3 eV tip-induced bending range of available states. This is near the 0.3 eV onset of the measured lowest unoccupied state, with a peak position of 0.36 eV, that is above the E_F (as shown in Fig. 5a), enabling Co_S to behave as an electron acceptor. Spatially-resolved charging ring formation as a function of applied bias is shown in Supplementary Fig. 15, where linescans taken across differential conductance maps from the defect center to outside the charging region highlight a shift to larger distances at more negative voltages. Outside the defect charging region, the substrate remains in a neutral state, which is verified with STS around pristine WS_2 regions (see Supplementary Fig. 16 for additional differential conductance mapping). While the charging process makes the identification of states closer to the VBM less straightforward, we note that, inside the charging ring, a state around the cobalt is observed. This state has the form of a d_{z^2} orbital as expected from the computed LDOS of the neutral cobalt defect in that energy range (Fig. 5c and Supplementary Fig. 9b). The better comparison is with the LDOS of the Co_S^{-1} as the defect should be charged within the ring. Theory predicts a reorganization of orbitals, an upward shift of the d_{z^2} and a change of symmetry going from C_s to C_{3v} when Co_S becomes negatively charged (see Supplementary Fig. 5). From this picture, we expect the d_{z^2} state for Co_S^{-1} to be 1 eV lower than the $d_{x^2-y^2}$ state from Co_S^0 . We found experimentally a value of 1.26 eV. If there is an upward shift of d_{z^2} when charged, it is smaller in experiment than in theory. This discrepancy could come from the influence of the dielectric environment of the graphene/SiC contacts that is not modeled in our WS_2 system in vacuum. In any case, next to the $d_{x^2-y^2}$, d_{yz} and d_{xz} Co state within the band gap, an additional Co d_{z^2} state is observed within the band gap (and 1.26 eV lower than the $d_{x^2-y^2}$ state) confirming the theoretical results that Co in WS_2 can lead to a two-level system of great interest as a QD.

DISCUSSION

We use HT computational screening to search for promising quantum defects in WS_2 . Based on a database gathering computed properties for 757 charged defects in WS_2 , we identify a handful of promising quantum defects with high brightness and in-gap defect states compatible with optical emission in the telecom or visible range. We fabricate the Co_S^0 defect, which we anticipate to exhibit brightness,

a spin-doublet ground state, and a computed ZPL in the telecom at 0.966 eV^{29,33,54}, through metal deposition and subsequent sulfur vacancy substitution by cobalt with an STM tip. STM and STS analysis indicates cobalt-related defect states within the band gap confirming the computational prediction and the interest of CoS as an OQD.

Our HT data indicates that fundamental electronic structure reasons make transition metal substitution on sulfur sites more likely to lead to a OQD with in-gap defect states that could emit in the telecom or visible than for the tungsten substitution. This motivates more efforts in the community along that direction. The fabrication process and HT computational screening used to identify CoS highlight the capability of combining HT screening and advanced synthesis techniques to identify and realize promising OQDs. This can be performed across a wide range of atomic species within 2D materials and other hosts with many yet to be experimentally realized, which can be executed for a number of different desired material properties, e.g., from catalysis to QIS.

METHODS

Scanning probe microscopy (SPM) measurements

All measurements were performed with a Createc GmbH scanning probe microscope operating under ultrahigh vacuum (pressure $< 2 \times 10^{-10}$ mbar) at liquid helium temperatures ($T < 6$ K). Either etched tungsten or platinum iridium tips were used during acquisition. Tip apexes were further shaped by indentations onto a gold substrate for subsequent measurements taken over a defective substrate. STM images are taken in constant-current mode with a bias applied to the sample. STS measurements were recorded using a lock-in amplifier with a resonance frequency of 683 Hz and a modulation amplitude of 5 mV. Band gaps from STS were determined by applying a linear fit to both the valence and conduction band edge, and the bottom of the band gap in $\log(dI/dV)$ ⁵⁵.

Sample preparation

Monolayer islands of WS₂ were grown on graphene/SiC substrates with an ambient pressure CVD approach (See Supplementary Fig. 17). A graphene/SiC substrate with 10 mg of WO₃ powder on top was placed at the center of a quartz tube, and 400 mg of sulfur powder was placed upstream. The furnace was heated to 900 °C and the sulfur powder was heated to 250 °C using a heating belt during synthesis. A carrier gas for process throughput was used (Ar gas at 100 sccm) and the growth time was 60 min. The CVD grown WS₂/MLG/SiC was further annealed *in vacuo* at 400 °C for 2 hours. WS₂ was sputtered with an argon ion gun (SPECS, IQE 11/35) that operated at 0.1 keV energy with 60° off-normal incidence at a pressure of 5×10^{-6} mbar and held at 600 °C. A rough measure of current (0.6×10^{-6} A) enabled the

argon ion flux to be estimated at $(1.5 \times 10^{13} \frac{\text{ions}}{\text{cm}^2 \text{s}})$, where the sample was irradiated for up to 30 seconds. Cobalt was deposited at a pressure of 1×10^{-9} mbar for 60 seconds with the sample held at 5 K.

Neural network and Gaussian process implementation

The acquisition software used for autonomous experimentation was gpSTS, which is a library for autonomous experimentation for scanning probe microscopy^{21,56}. An Intel Xeon E5-2623 v3 CPU with 8 cores and 64 GB of memory combined with a Tesla K80 with 4992 CUDA cores was used for training the neural network. Training data for WS_2 and V_S was combined with Co_S spectra obtained from an extended autonomous run.

First-principles calculations

We considered 57 elements that could substitute for W and S in the construction of a WS_2 quantum defect database, as highlighted in the periodic table in Supplementary Fig. 1. This collection covers the majority of the elements except the rare-earth elements and noble gases. All defect computations were performed at DFT level using automatic defect workflows that are implemented in ATOMATE software package^{57–59}. The defect structure generations and the formation energy computations are performed using PYCDT. The DFT calculations were performed using Vienna Ab-initio Simulation Package (VASP)^{60,61} and the projector-augmented wave (PAW) method⁶² with the Perdew-Burke-Ernzerhof (PBE) functional⁶³. Each charged defect is simulated in a 144-atom orthorhombic supercell and with a vacuum of approximately 14 Å. A plane-wave basis energy cutoff of 520 eV was used and the Brillouin zone is sampled using Γ point only. The defect structures were optimized at a fixed volume until the forces on the ions are smaller than 0.01 eV/Å. The charge states of each defect are determined by considering all the oxidation states of the elements documented in the ICSD database⁵⁸ and taking into account the formal charges in WS_2 (W^{4+} and S^{2-}). The total energy of the charged defects were further corrected to overcome the finite-size effect using the method of Komsa et al.^{64,65} as implemented in SLABCC⁶⁶.

The above procedures generated overall 757 substitutional charged defects in monolayer WS_2 . Based on the defect formation energy, we first identified 260 charged defects that are thermodynamically stable, meaning their charge states are accessible in a certain E_F range. Of these, 89 defects exhibit singlet ground states, 94 show doublet character, 48 are triplets, and 16 are in higher states. Among these stable defects, we further search for the ones that possess two in-gap, localized levels that would enable the optical intra-defect transition. The localization is defined using inverse participation ratio (IPR) as detailed below. We considered levels with IPR larger than 0.05 as localized states (bulk-like states in general have IPR smaller than 0.01 in WS_2). This trimmed down the list to 143 candidates, among which 112 have non-singlet ground states. The classification of singlets and multiplets is based on the

electronic structure of the defect. In this case, the singlets and multiplets refer to the total magnetic quantum number of the unpaired electrons. Thus, defects with all electrons paired are classified as singlet, while those with one or two paired electrons are classified as doublet, triplet, etc. We note that due to limitations of Kohn-Sham (KS) DFT and possibility of spin contamination for spin-polarized systems, more powerful methods such as spin-flip Bethe-Salpeter are required in general to rigorously determine the total spin S^{67} . Finally, we screened out the ones that would emit at telecom wavelength with reasonable brightness. The emission wavelength is approximated using the single-particle KS energy difference using the single-shot PBE0 incorporating 7% of Fock exchange. We refrained from applying potential corrections at this stage as the KS energy difference is largely unaffected by the electrostatic finite-size effect. The brightness of the optical transition is approximated by the transition dipole moment (TDM) as detailed below. To search for the most relevant transitions, we consider the transitions that give the smallest energy difference, while also allowing an energy window of up to 100 meV to take into account the errors and band degeneracy. We then identified the transition with the largest TDM as the most relevant transition. The above procedures recommend 17 non-singlet candidates that emit at least 750 meV with a TDM of 3 D, as shown in Supplementary Table 1.

The localization of an orbital is described using the IPR. For a given KS State, the IPR is evaluated based on the probabilities of finding an electron with an energy E_i close to an atomic site α^{68-70} :

$$\chi(E_i) = \frac{\sum_{\alpha} \rho_{\alpha}^2(E_i)}{[\sum_{\alpha} \rho_{\alpha}(E_i)]^2}, \quad (1)$$

where the summation runs over all atomic sites α . The participation ratio χ^{-1} stands for the number of atomic sites that confine the wave function. Thus, a larger (smaller) IPR indicate a localized (delocalized) state. IPR is unitless ranging between 0 to 1. We computed IPR using VASP PROCAR. The optical transition dipole moment was evaluated by the PYVASPWFC code based on the single-particle wavefunction calculated at the PBE level⁷¹. The transition dipole moment is written as:

$$\mu_k = \frac{i\hbar}{(\epsilon_{f,k} - \epsilon_{i,k})m} \langle \psi_{f,k} | \mathbf{p} | \psi_{i,k} \rangle, \quad (2)$$

where \hbar is the Planck constant, $\epsilon_{i,k}$ and $\epsilon_{f,k}$ are the eigenvalues of the initial and final states, m is the electron mass, ψ_i and ψ_f are the initial and final wavefunctions, and \mathbf{p} is the momentum operator.

For selected substitutional defects, we carried out the fully self-consistent hybrid functional (PBE0) calculations including structural relaxations. In line with the single-shot PBE0 calculations and following previous work³⁷, we described the defect levels using the mixing parameter $\alpha = 0.07$ for the Fock exchange, which generally satisfies the Koopmans' condition for localized defects in monolayer WS₂. On the other hand, we used $\alpha = 0.22$ for the pristine WS₂ to determine the band-edge position. The alignment of defect levels with respect to the band edges was then achieved through the vacuum level which serves a

common reference level. Spin-orbit coupling (SOC) is taken into account unless otherwise specified. We used a planewave cutoff energy of 400 eV and a $2 \times 2 \times 1$ **k**-point mesh for ground-state calculations. The zero-phonon line was assessed using a single Γ point by imposing occupation constraints (constrained DFT²⁸). For charged defects, the total energies are subject to finite-size effects and were corrected by the method of Komsa et al.^{64,65} as implemented in SLABCC⁶⁶, whereas the single-particle KS levels were corrected by the potential correction scheme (SCPC) of Chagas da Silva et al.⁷². The simulated STM images were plotted at a constant height of 3.5 Å above the surface using the STM-2DScan package⁷³ based on the Tersoff-Hamann theory⁷⁴.

Data availability

The computational dataset used in this work has been made publicly available at <https://defectgenome.org>. Additional data that support the findings of this study are available from the corresponding authors on request.

Code availability

The code used for the findings of this study are available from the corresponding authors on request.

REFERENCES

-
- [1] Maletinsky, P. et al. A robust scanning diamond sensor for nanoscale imaging with single nitrogen-vacancy centres. *Nat. Nanotechnol.* **7**, 320 (2012).
 - [2] Bradley, C. E. et al. A Ten-Qubit Solid-State spin register with quantum memory up to one minute. *Phys. Rev. X* **9**, 031045 (2019).
 - [3] Pompili, M. et al. Realization of a multinode quantum network of remote solid-state qubits. *Science* **372**, 259 (2021).
 - [4] Wolfowicz, G. et al. Quantum guidelines for solid-state spin defects. *Nat. Rev. Mater.* **6**, 906 (2021).
 - [5] Bassett, L. C., Alkauskas, A., Exarhos, A. L., & Fu, K.-M. C. Quantum defects by design. *Nanophotonics* **8**, 1867 (2019).
 - [6] Atatüre, M., Englund, D., Vamivakas, N., Lee, S.-Y., & Wrachtrup, J. Material platforms for spin-based photonic quantum technologies. *Nat. Rev. Mater.* **3**, 38 (2018).
 - [7] Sukachev, D. D. et al. Silicon-Vacancy spin qubit in diamond: A quantum memory exceeding 10 ms with Single-Shot state readout. *Phys. Rev. Lett.* **119**, 223602 (2017).

- [8] Bourgeois, E., Gulka, M., & Nesladek, M. Photoelectric detection and quantum readout of nitrogen-vacancy center spin states in diamond. *Adv. Opt. Mater.* **8**, 1902132 (2020).
- [9] Stern, H. L. et al. Room-temperature optically detected magnetic resonance of single defects in hexagonal boron nitride. *Nat. Commun.* **13**, 618 (2022).
- [10] Kianinia, M., Xu, Z.-Q., Toth, M., & Aharonovich, I. Quantum emitters in 2D materials: emitter engineering, photophysics, and integration in photonic nanostructures. *Appl. Phys. Rev.* **9**, 011306 (2022).
- [11] Lin, Z. et al. Defect engineering of two-dimensional transition metal dichalcogenides. *2D Mater.* **3**, 022002 (2016).
- [12] Manzeli, S., Ovchinnikov, D., Pasquier, D., Yazyev, O. V., & Kis, A. 2D transition metal dichalcogenides. *Nat. Rev. Mater.* **2**, 1 (2017).
- [13] Li, C. et al. Engineering graphene and TMDs based van der waals heterostructures for photovoltaic and photoelectrochemical solar energy conversion. *Chem. Soc. Rev.* **47**, 4981 (2018).
- [14] Ugeda, M. M. et al. Observation of topologically protected states at crystalline phase boundaries in single-layer WSe₂. *Nature Communications*, vol. 9, p. 3401, Aug 2018.
- [15] Schuler, B. et al. Electrically driven photon emission from individual atomic defects in monolayer WS₂. *Sci. Adv.* **6**, eabb5988 (2020).
- [16] Schuler, B. et al. Large spin-orbit splitting of deep in-gap defect states of engineered sulfur vacancies in monolayer WS₂. *Phys. Rev. Lett.* **123**, 076801 (2019).
- [17] Montblanch, A. R. P., Barbone, M., Aharonovich, I., Atatüre, M., & Ferrari, A. C. Layered materials as a platform for quantum technologies. *Nat. Nanotechnol.* **18**, 555 (2023).
- [18] Ye, M., Seo, H., & Galli, G. Spin coherence in two-dimensional materials. *npj Comput. Mater.* **5**, 44 (2019).
- [19] Kanai, S. et al., Generalized scaling of spin qubit coherence in over 12,000 host materials. *Proc. Natl. Acad. Sci. U.S.A.* **119**, e2121808119 (2022).
- [20] Schuler, B. et al. How substitutional point defects in two-dimensional WS₂ induce charge localization, spin-orbit splitting, and strain. *ACS Nano* **13**, 10520 (2019).
- [21] Thomas, J. C. et al. Autonomous scanning probe microscopy investigations over WS₂ and Au{111}. *npj Comput. Mater.* **8**, 99 (2022).

- [22] Barja, S. et al. Identifying substitutional oxygen as a prolific point defect in monolayer transition metal dichalcogenides. *Nat. Commun.* **10**, 3382 (2019).
- [23] Cochrane, K. A. et al. Spin-dependent vibronic response of a carbon radical ion in two-dimensional WS₂. *Nat. Commun.* **12**, 7287 (2021).
- [24] Stolz, S. et al. Layer-dependent schottky contact at van der waals interfaces: V-doped WSe₂ on graphene,” *npj 2D Mater. Appl.* **6**, 66 (2022).
- [25] Gali, A. Ab initio theory of the nitrogen-vacancy center in diamond. *Nanophotonics* **8**, 1907 (2019).
- [26] Freysoldt, C. et al. First-principles calculations for point defects in solids. *Rev. Mod. Phys.* **86**, 253 (2014).
- [27] Dreyer, C. E., Alkauskas, A., Lyons, J. L., Janotti, A. , & Van de Walle, C. G. First-principles calculations of point defects for quantum technologies. *Annu. Rev. Mater. Res.* **48**, 1 (2018).
- [28] Ivády, V., Abrikosov, I. A., & Gali, A. First principles calculation of spin-related quantities for point defect qubit research. *npj Comput. Mater.***4**, 76 (2018).
- [29] Tsai, J.-Y., Pan, J., Lin, H., Bansil, A., & Yan, Q. Antisite defect qubits in monolayer transition metal dichalcogenides. *Nat. Commun.* **13**, 492 (2022).
- [30] Frey, N. C., Akinwande, D., Jariwala, D., & Shenoy, V. B. Machine learning-enabled design of point defects in 2D materials for quantum and neuromorphic information processing. *ACS Nano* **14**, 13406 (2020).
- [31] Ping, Y. & Smart, T. J. Computational design of quantum defects in two-dimensional materials. *Nat. Comput. Sci.* **1**, 646 (2021).
- [32] Narang, P., Ciccarino, C. J., Flick, J., & Englund, D. Quantum materials with atomic precision: artificial atoms in solids: ab initio design, control, and integration of single photon emitters in artificial quantum materials. *Adv. Func. Mater.* **29** 1904557 (2019).
- [33] Li, S., Thiering, G., Udvarhelyi, P., Ivády, V., & Gali, A. Carbon defect qubit in two-dimensional WS₂. *Nat. Commun.* **13**, 1 (2022).
- [34] Peng, J. et al. Human- and machine-centred designs of molecules and materials for sustainability and decarbonization. *Nat. Rev. Mater.* **7**, 991 (2022).
- [35] Gupta, S., Yang, J.-H., & Yakobson, B. I. Two-level quantum systems in two-dimensional materials for single photon emission. *Nano Lett.* **19**, 408 (2019).

- [36] Xiong, Y., Mathew, M., Griffin, S. M., Sipahigil, A., & Hautier, G. Midgap state requirements for optically active quantum defects. *Mater. Quantum. Technol.* **4**, 013001 (2024).
- [37] Chen, W., Griffin, S. M., Rignanese, G.-M., & Hautier, G. Nonunique fraction of Fock exchange for defects in two-dimensional materials. *Phys. Rev. B* **106**, L161107 (2022).
- [38] Xiong, Y. et al. High-throughput identification of spin-photon interfaces in silicon. *Sci. Adv.* **9**, eadh8617 (2023).
- [39] Hensen, B. et al. Loophole-free bell inequality violation using electron spins separated by 1.3 kilometres. *Nature* **526**, 682 (2015).
- [40] Higginbottom, D. B. et al. Optical observation of single spins in silicon. *Nature* **607**, 266 (2022).
- [41] Anderson, C. P., & Awschalom, D. D. Embracing imperfection for quantum technologies. *Phys. Today* **76**, 26 (2023).
- [42] Loh, L. et al. Impurity-induced emission in Re-doped WS₂ monolayers. *Nano Lett.* **21**, 5293 (2021).
- [43] Qin, Z. et al. Growth of Nb-doped monolayer WS₂ by liquid-phase precursor mixing. *ACS Nano* **13**, 10768 (2019).
- [44] Zhang, F. et al. Monolayer vanadium-doped tungsten disulfide: A room-temperature dilute magnetic semiconductor. *Adv. Sci.* **7**, 2001174 (2020).
- [45] Han, A. et al. One-step synthesis of single-site vanadium substitution in 1T-WS₂ monolayers for enhanced hydrogen evolution catalysis. *Nat. Commun.* **12**, 709 (2021).
- [46] Lei, Y. et al. Graphene and beyond: Recent advances in two-dimensional materials synthesis, properties, and devices. *ACS Nanosci. Au* **2**, 450 (2022).
- [47] Pike, N. A. et al. Origin of the counterintuitive dynamic charge in the transition metal dichalcogenides. *Phys. Rev. B* **95**, 201106 (2017).
- [48] Zhou, J. et al. Near-field coupling with a nanoimprinted probe for dark exciton nanoimaging in monolayer WSe₂. *Nano Lett.* **23**, 4901 (2023).
- [49] Rossi, A. et al. WS₂ band gap renormalization induced by Tomonaga Luttinger liquid formation in mirror twin boundaries. Preprint at <https://arxiv.org/abs/2301.02721> (2023).
- [50] Kandel S. A. & Weiss, P. S. Binding and mobility of atomically resolved cobalt clusters on molybdenum disulfide. *J. Phys. Chem. B* **105**, 8102 (2001).

- [51] Tang, W. et al. Identically sized Co quantum dots on monolayer WS₂ Featuring Ohmic Contact. *Phys. Rev. Applied* **13**, 024003 (2020).
- [52] Teichmann, K. et al. Controlled charge switching on a single donor with a scanning tunneling microscope. *Phys. Rev. Lett.* **101**, 076103 (2008).
- [53] Subramanian, S. et al. Tuning transport across MoS₂/graphene interfaces via as-grown lateral heterostructures. *npj 2D Mater. Appl.* **4**, 9 (2020).
- [54] Lee, Y., Hu, Y., Lang, X., Kim, D., Li, K., Ping, Y., Fu, K.-M. C., & Cho, K. Spin-defect qubits in two-dimensional transition metal dichalcogenides operating at telecom wavelengths. *Nature Communications* **13**, 7501 (2022).
- [55] Tang, S. et al. Quantum spin hall state in monolayer 1T'-WTe₂. *Nat. Phys.* **13**, 683 (2017).
- [56] Noack, M. M. et al. gpCAM. <https://github.com/lbl-camera/gpCAM> (2022).
- [57] Mathew, K. et al. Atomate: A high-level interface to generate, execute, and analyze computational materials science workflows. *Comput. Mater. Sci.* **139**, 140 (2017).
- [58] Ong, S. P. et al. Python materials genomics (pymatgen): A robust, open-source python library for materials analysis," *Comput. Mater. Sci.* **68**, 314 (2013).
- [59] Jain, A. et al. Commentary: The Materials Project: A materials genome approach to accelerating materials innovation. *APL Mater.* **1**, 11002 (2013).
- [60] Kresse, G. & Furthmüller, J. Efficiency of ab-initio total energy calculations for metals and semi-conductors using a plane-wave basis set. *Comput. Mater. Sci.* **6**, 15 (1996).
- [61] Kresse G. & Furthmüller, J. Efficient iterative schemes for ab initio total-energy calculations using a plane-wave basis set. *Phys. Rev. B* **54**, 11169 (1996).
- [62] Blöchl, P. E. Projector augmented-wave method. *Phys. Rev. B* **50**, 17953 (1994).
- [63] Perdew, J. P., Burke, K. & Ernzerhof, M. Generalized gradient approximation made simple. *Phys. Rev. Lett.* **77**, 3865 (1996).
- [64] Komsa, H.-P. & Pasquarello, A. Finite-size supercell correction for charged defects at surfaces and interfaces. *Phys. Rev. Lett.* **110**, 095505 (2013).
- [65] Komsa, H.-P., Berseneva, N., Krashennnikov, A. V., & Nieminen, R. M. Charged point defects in the flatland: Accurate formation energy calculations in two-dimensional materials. *Phys. Rev. X* **4**, 031044 (2014).

- [66] Farzalipour Tabriz, M., Aradi, B., Frauenheim, T., & Deák, P. SLABCC: Total energy correction code for charged periodic slab models. *Comput. Phys. Commun.* **240**, 101 (2019).
- [67] Barker, B. A. & Strubbe, D. A. Spin-flip Bethe-Salpeter equation approach for ground and excited states of open-shell molecules and defects in solids. Preprint at <http://arxiv.org/abs/2207.04549>. (2022).
- [68] Wegner, F. Inverse participation ratio in $2+\epsilon$ dimensions. *Zeitschrift für Phys. B Condens. Matter* **36**, 209 (1980).
- [69] Pashartis C. & Rubel, O. Localization of electronic states in III-V semiconductor alloys: A comparative study. *Phys. Rev. Applied* **7**, 064011 (2017).
- [70] Konstantinou, K., Mocanu, F. C., Lee, T.-H., & Elliott, S. R. Revealing the intrinsic nature of the mid-gap defects in amorphous $\text{Ge}_2\text{Sb}_2\text{Te}_5$. *Nat. Commun.* **10**, 3065 (2019).
- [71] Zheng, Q. Vasp band unfolding. <https://github.com/QijingZheng/VaspBandUnfolding> (2018).
- [72] Chagas da Silva, M. et al. Self-consistent potential correction for charged periodic systems. *Phys. Rev. Lett.* **126**, 076401 (2021).
- [73] Leung, S. Stm 2d scan. https://github.com/ShuangLeung/STM_2DScan (2020).
- [74] Tersoff, J. & Hamann, D. R. Theory of the scanning tunneling microscope. *Phys. Rev. B* **31**, 805 (1985).

Acknowledgements

This work was supported by the U.S. Department of Energy, Office of Science, Basic Energy Sciences in Quantum Information Science under Award Number DE-SC0022289. This work was supported as part of the Center for Novel Pathways to Quantum Coherence in Materials, an Energy Frontier Research Center funded by the U.S. Department of Energy, Office of Science, Basic Energy Sciences. Work was performed at the Molecular Foundry and at the Advanced Light Source supported by the Office of Science, Office of Basic Energy Sciences, of the U.S. Department of Energy under contract no. DE-AC02-05CH11231. S.K and J.A.R. acknowledge support from the National Science Foundation Division of Materials Research (NSF-DMR) under awards 2002651 and 2011839. N.K. and D.A.S acknowledge support from the National Science Foundation award DMR-2144317, and the Merced nAnomaterials Center for Energy and Sensing (MACES), a NASA-funded research and education center, under award

NNH18ZHA008CMIROG6R. B.A.B. was supported by the U.S. Department of Energy, Office of Science, Basic Energy Sciences, CTC and CPIMS Programs, under Award DE-SC0019053. This research used resources of the National Energy Research Scientific Computing Center, a DOE Office of Science User Facility supported by the Office of Science of the U.S. Department of Energy under Contract No. DE-AC02-05CH11231 using NERSC award BES-ERCAP0020966. Additional computational resources were provided by the Multi-Environment Computer for Exploration and Discovery (MERCED) cluster at UC Merced, funded by National Science Foundation Grant No. ACI-1429783.

Author Contributions

G.H., A.W.-B, J.C.T., S.G., and A. R. (Archana Raja) conceived the overall project. W.C. (Wei Chen), Y.X., B.A.B., W. C. (Weiru Chen), N.K., S.G., D.A.S., G.-M.R., and G.H. performed the theoretical simulations along with compiling the database for quantum defect search. J.C.T, J.Z., and A.R. (Antonio Rossi) performed STM/STS experiments and subsequent analysis with support from E.S.B., A.S., D.F.O., E.R., A.R. (Archana Raja), and A.W.-B. J.C.T. and M.M.N. implemented autonomous experimentation. Z.Y., D.Z., S.K., J.A.R., and M.T. carried out sample growth. All authors discussed the results and contributed towards the manuscript.

Competing interests

The authors declare that they have no competing interests.

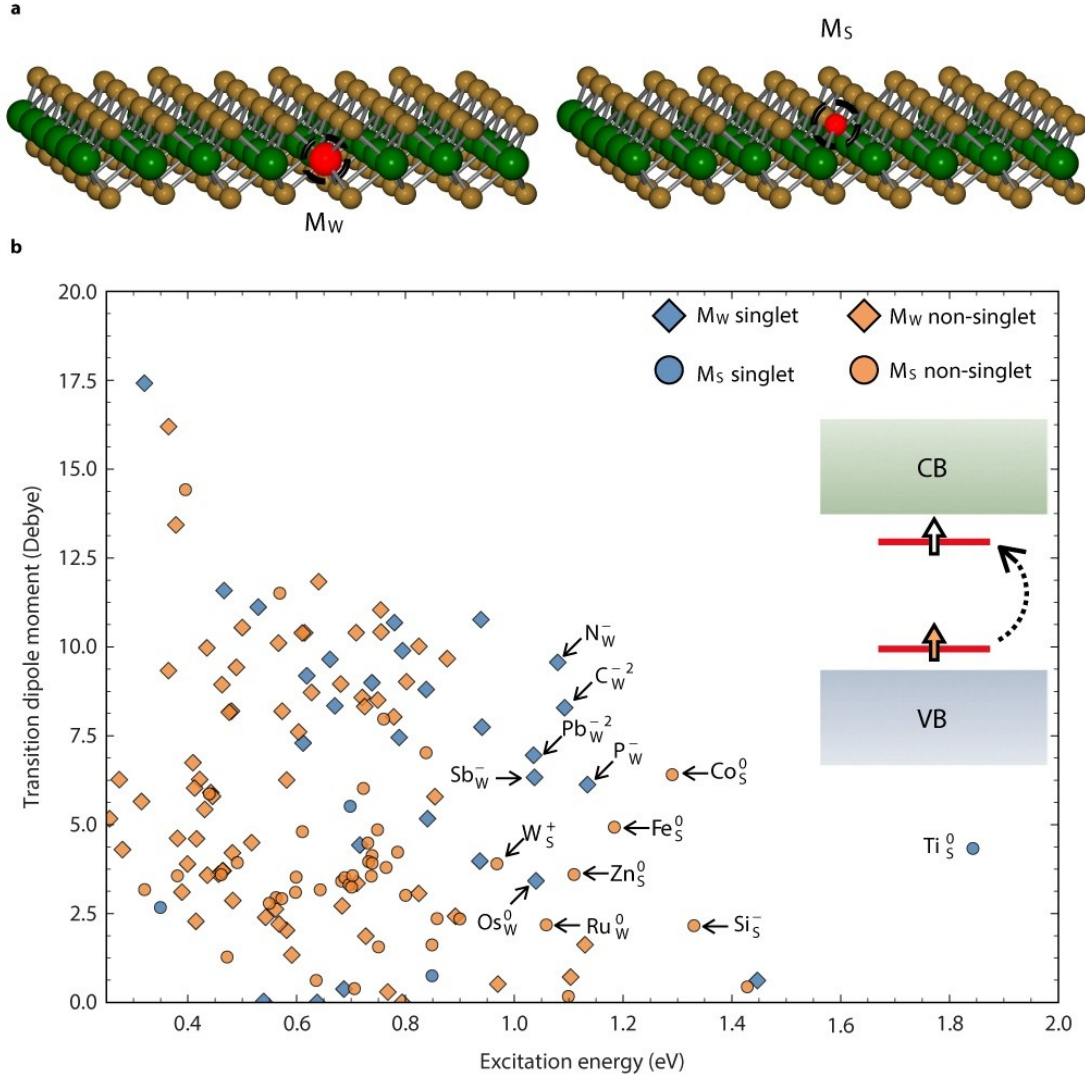


Fig. 1: Two-Level Quantum Defect Screening in WS₂. **a** Two defect configurations that are considered in this work: substitution on W site (M_W, red) is shown on the left and on S site (M_S, red) is depicted on the right. W atoms are colored green and S atoms are displayed in yellow. **b** Transition dipole moment vs. single-particle excitation energy at the single-shot PBE0. The marker and color scheme stand for the defect structure and whether the ground state is singlet or not. Each point stands for a charge defect that is thermodynamically stable within a certain Fermi level (E_F) range in the band gap, and with electronic structures that possess two localized defect levels within the band gap, as shown in the inset. Below the conduction band (CB, light green) and above the valence band (VB, light blue), a filled state (orange arrow) to empty state (white arrow) transition is shown.

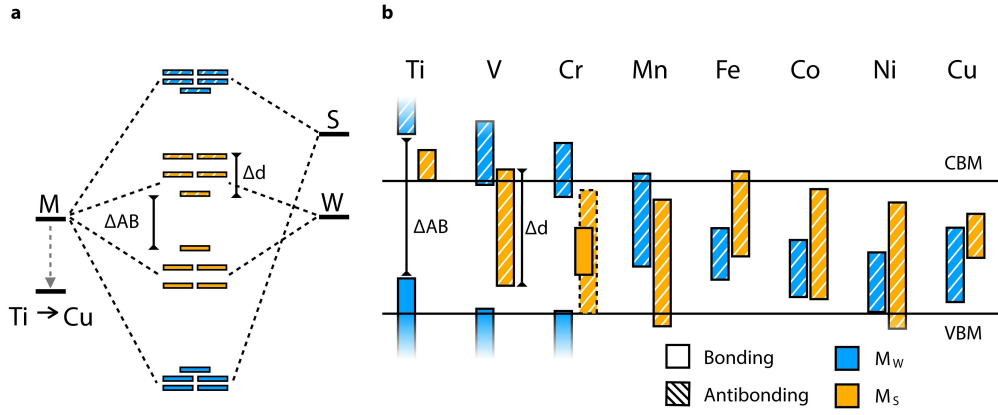


Fig. 2: Molecular orbital trend within the 3d transition metal series for M_S and M_W defects. a The molecular orbital diagram shows the splitting between anti-bonding and bonding state (Δ_{AB}) as well as the splitting with d orbitals (Δ_d) for a typical M_W and M_S defect. **b** A schematic of the bonding and anti-bonding state for different 3d transition metals in M_W (blue) and M_S (yellow) positions. The conduction band minimum (CBM) and valence band maximum (VBM) are drawn as black lines.

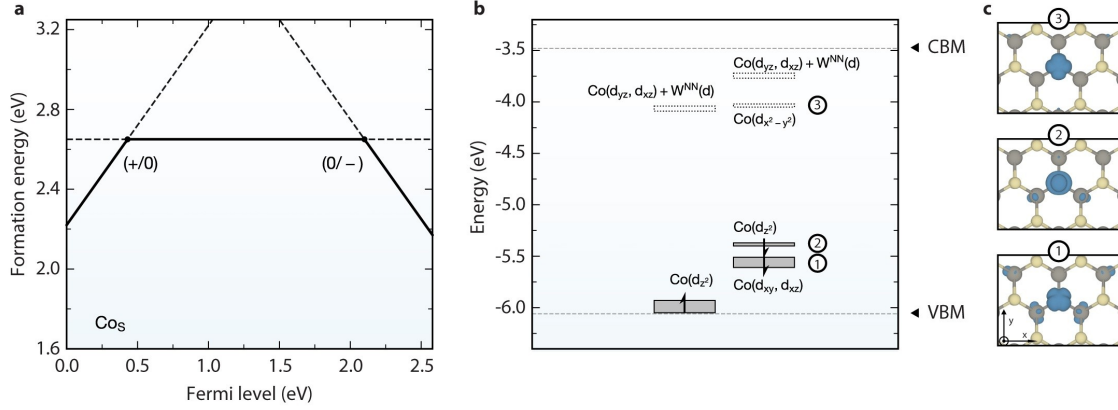


Fig. 3: Thermodynamic charge transition levels and electronic structure of CoS. **a** Formation energy of CoS as a function of Fermi level for the neutral and the two charged states. The charge transition levels, i.e., (+/0) and (0/-), are referenced to the band-edge positions of pristine WS₂ as obtained with PBE0 incorporating 22% of Fock exchange PBE0(0.22). **b** Orbital diagram of the localized defect states for neutral CoS. Resonant states within the valence band and conduction band manifolds are not depicted. The characters of the localized states are indicated by the specific *d* orbitals of the Co atom [e.g., Co(*d_{z²}*) as the highest occupied state in the minority channel] and, if any, the *d* orbitals of the W atoms in the nearest neighbor (W^{NN}). The occupied (unoccupied) states are shown by the filled (empty) rectangles, the height of which indicates the degree of dispersion. The localized electrons in the majority (minority) channel are indicated by the arrows pointing up (down). The band-edge positions (in horizontal dashed lines) refer to those of the pristine WS₂ obtained with PBE0(0.22). Energies are referenced to the vacuum level. SOC is not taken into account for the localized defect states. **c** Top view of the charge density (in blue) for the three CoS⁰ defect states as indicated in **b**. The W and S atoms are represented by the grey and yellow spheres, respectively. The isovalue is 0.001 e/Å³.

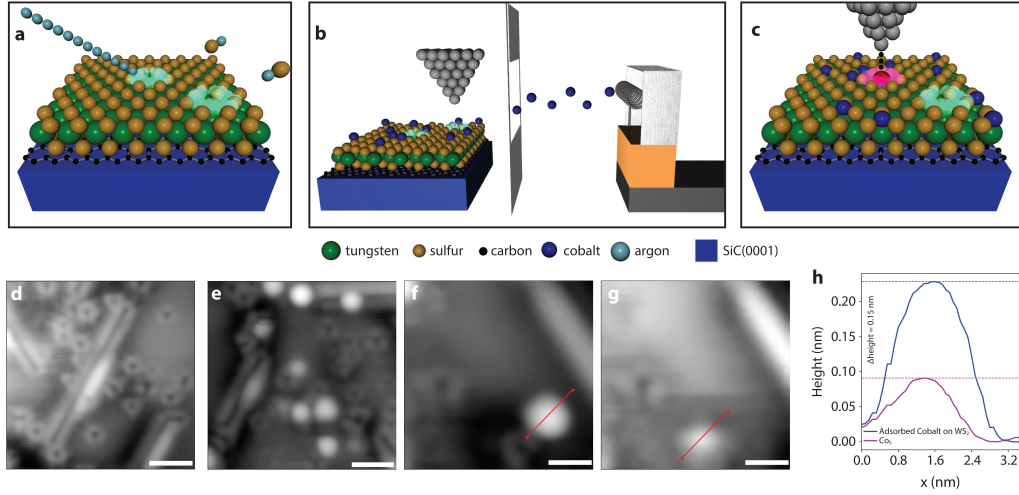


Fig. 4: CoS Defect Formation and Characterization. **a** The process of forming a high density of V_S , **b** low-temperature deposition of Co atoms *in situ*, and **c** subsequent placement into a sulfur vacancy (V_S) with the assistance of the STM probe that is used to selectively manipulate atoms at voltage ranges below -1.3 V is shown schematically. Corresponding scanning tunneling micrographs that capture $WS_2/Gr/SiC(0001)$ **d** after defect introduction via Ar^+ bombardment and **e** post Co deposition are plotted ($I_{tunnel} = 30$ pA, $V_{sample} = 1.2$ V). Scale bars, 2 nm. STM images **f** before a voltage excitation and **g** after Co substitution within an identified V_S are also shown ($I_{tunnel} = 30$ pA, $V_{sample} = 1.2$ V, $V_{excitation} = -2.1$ V). Scale bars, 2 nm. I_{tunnel} is the tunneling current, V_{sample} is the sample bias voltage, and $V_{excitation}$ is the applied excitation voltage. **h** The apparent height difference of CoS compared to adsorption atop as-grown WS_2 is measured to be 0.15 nm, taken from linescans across both **f** (maxima shown with blue dashed line) and **g** (maxima shown with magenta dashed line) red highlighted regions.

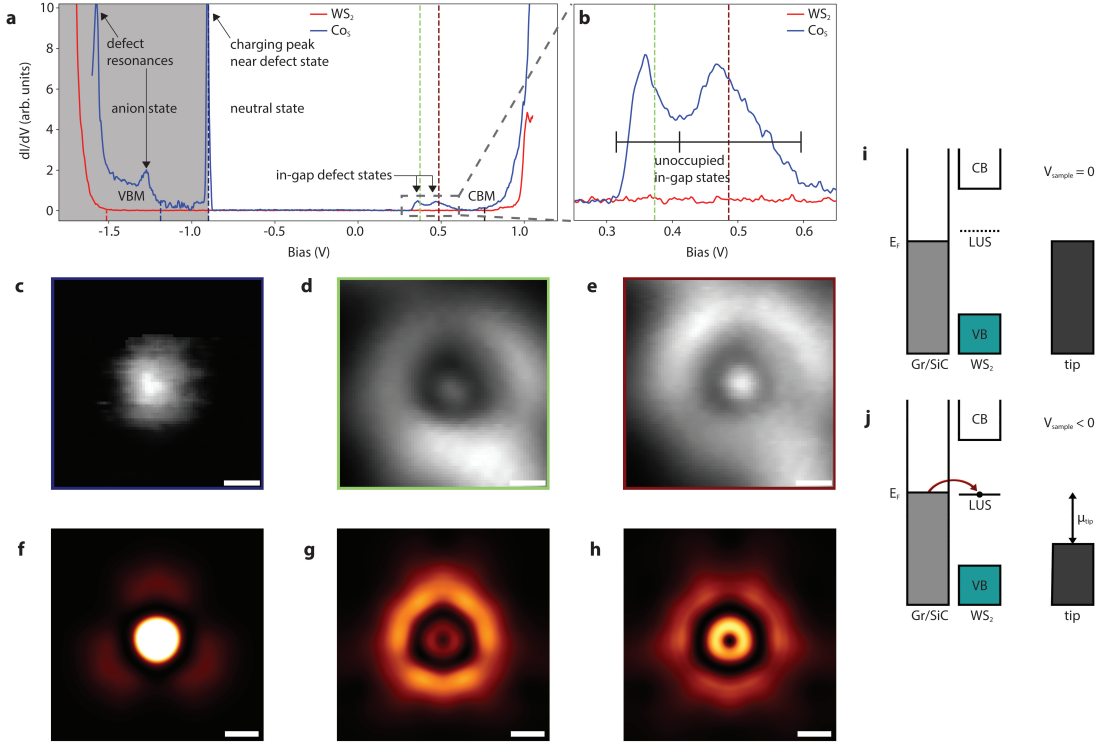


Fig. 5: Experimental and Simulated CoS Scanning Tunneling Spectroscopy. **a** Scanning tunneling spectra (STS) recorded on a CoS defect and the as-grown WS_2 monolayer on graphene ($V_{modulation} = 5$ mV), where defect resonances, VBM and CBM onsets, in-gap states, and the shift between neutral (white background) to an anionic charge state (gray background) are labeled. $V_{modulation}$ is the bias modulation. **b** In-gap states identified are located at peak maxima of 0.36 eV and 0.47 eV, each with a full-width half maximum near 0.045 eV. Peak widths are broadened due to vibronic excitations (black lines). Differential conductance (dI/dV) imaging maps over the defect are depicted at **c** -0.9 eV (vertical black dashed line in **a**), **d** 0.373 eV (vertical green dashed lines in **a**, **b**), and **e** 0.486 eV (vertical red dashed lines in **a**, **b**) ($V_{modulation} = 5$ mV), showing CoS orbital geometries. Scale bars, 0.25 nm. **f-h** Simulated STS maps using PBE0 over CoS orbitals identifying energy range densities near experimentally measured values. Scale bars, 0.25 nm. Isocontour value, $7 \times 10^{-6} \text{ \AA}^{-3}$. A charging peak is identified in **a**, where the **i** lowest unoccupied CoS^0 state becomes **j** resonant with the E_F of the substrate and an electron is donated to the lowest unoccupied state (LUS) at sufficient V_{sample} (or equivalent tip potential, μ_{tip}) produce the CoS^{-1} defect. Both **c** and **f** are representative of the CoS^{-1} orbital densities collected at the specified energy (the charging ring onset in **c** is removed for clarity).

Supplementary Information for A substitutional quantum defect in WS₂ discovered by high-throughput computational screening and fabricated by site-selective STM manipulation

John C. Thomas^{1,2,3*†}, Wei Chen^{4†}, Yihuang Xiong^{3†}, Bradford A. Barker⁵, Junze Zhou¹,
Weiru Chen³, Antonio Rossi^{1,2,6}, Nolan Kelly⁵, Zhuohang Yu^{7,8}, Da Zhou⁹, Shalini Kumari^{7,8},
Edward S. Barnard¹, Joshua A. Robinson^{7,8,9,10}, Mauricio Terrones^{7,8,9,10}, Adam
Schwartzberg¹, D. Frank Ogletree¹, Eli Rotenberg⁶, Marcus M. Noack¹¹, Sinéad Griffin^{1,2},
Archana Raja^{1,2}, David A. Strubbe⁵, Gian-Marco Rignanes⁴, Alexander Weber-Bargioni^{1,2*},
and Geoffroy Hautier^{3*}

¹*Molecular Foundry, Lawrence Berkeley National Laboratory, Berkeley, CA 94720, United States of America*

²*Materials Sciences Division, Lawrence Berkeley National Laboratory, Berkeley, CA, United States of America*

³*Thayer School of Engineering, Dartmouth College, Hanover, NH 03755, USA*

⁴*Institute of Condensed Matter and Nanoscience, Université catholique de Louvain, Louvain-la-Neuve 1348, Belgium*

⁵*Department of Physics, University of California, Merced, Merced, CA 95343, USA*

⁶*Advanced Light Source, Lawrence Berkeley National Laboratory, Berkeley, CA 94720, United States of America*

⁷*Department of Materials Science and Engineering, The Pennsylvania State University, University Park, PA 16802 United States of America*

⁸*Center for Two-Dimensional and Layered Materials, The Pennsylvania State University, University Park, PA, 16802 United States of America*

⁹*Department of Physics, The Pennsylvania State University, University Park, PA, 16802 United States of America*

¹⁰*Department of Chemistry, The Pennsylvania State University, University Park, PA, 16802 United States of America*

¹¹*Applied Mathematics and Computational Research Division, Lawrence Berkeley National Laboratory, Berkeley, CA 94720, United States of America*

*jthomas@lbl.gov, afweber-bargioni@lbl.gov, geoffroy.hautier@dartmouth.edu

†These authors contributed equally.

SUPPLEMENTARY NOTES

1I Autonomous Experimentation

A Gaussian process (GP) model can be defined for a given dataset, $D = \{x_i, y_i\}$, which takes into account $y(x) = f(x) + \varepsilon(x)$, where x are the positions in some input or parameter space, y is the associated noisy function evaluation, and $\varepsilon(x)$ represents the noise term. The variance-covariance matrix Σ of the prior Gaussian probability distribution is defined by Matérn kernel functions $k(x_i, x_j; \phi)$, where ϕ is the

set of hyperparameters found by maximizing the marginal log-likelihood of the data¹. A predictive mean and variance can then be defined given a Gaussian probability distribution with a set of optimized hyperparameters, which can be further used to find the next optimal point measurements in the GP-driven data acquisition loop. For the results presented, an acquisition function that collects points to reduce uncertainty and improve the statistical model (exploration mode) was used. Drift was corrected during the autonomous experiment, where x - y offsets were calculated after each spectral loop and applied to the dataset.

2| 1D Convolutional Neural Network

Spectra for WS₂ and V_S were taken from Thomas et al. and used during training¹. The one-dimensional convolutional neural network (CNN) chosen makes use of two convolution layers, one dropout layer, and one fully connected linear layer. We use an 80/20 train/validation split ratio on 394 individually and separately acquired scanning tunneling spectra, consisting of 45 CoS, 158 V_S, and 191 WS₂ spectra. Validation data is further split (60/40 ratio) for a portion to be used during training, which yields an estimate of the model's skill, and a test set used on unbiased data after training. The softmax of the trained model is then used after training to obtain point STS class probabilities. All convolutional layers make use of a 1×3 kernel to compute the sliding dot product and produce spectral feature maps at each layer (stride 1, padding 1). This is followed by batch normalization, a rectified linear unit activation, and a maxpooling layer. The Adam algorithm² with a learning rate of 10^{-4} and computed cross-entropy loss for optimization are used during training to automatically identify spectral features. Spectra for WS₂, V_S, and CoS that are unseen by the trained model are used for test data. The CNN architecture chosen uses shared weights to reduce the number of trainable parameters and extract spectral features on the pixel level.

SUPPLEMENTARY TABLE

Defect Database:

Defect	Total spin	Δ KS (eV)	TDM (Debye)
Br_W^0	1/2	0.854	5.79
Sc_S^0	1/2	0.8	3.01
Sb_W^-	0	1.037	6.33
Rb_W^-	1	0.825	10.01
Te_W^-	1/2	0.778	8.03
S_W^0	0	0.939	10.77
P_W^-	0	1.134	6.13
Ir_W^+	0	0.84	5.17
As_W^-	0	0.941	7.74
Pb_W^{-2}	0	1.035	6.95
C_W^{-2}	0	1.093	8.29
K_W^-	1	0.877	9.67
Ca_W^0	1	0.755	10.42
Ca_W^{-2}	0	0.794	9.89
Mg_S^+	1/2	0.786	4.23
N_W^-	0	1.08	9.56
Ru_W^0	0	0.937	3.97
Ru_W^+	1/2	0.824	3.06
Co_S^0	1/2	1.29	6.41
Bi_W^-	0	0.838	8.8
W_S^+	1/2	0.968	3.9
Vac_W^{-2}	1	0.76	7.97
Rh_W^-	0	0.788	7.45
Os_W^0	0	1.04	3.42
Fe_S^0	1	1.184	4.93
Sr_W^0	1	0.754	11.04
Sr_W^{-2}	0	0.78	10.68
Na_W^-	1	0.802	9.02
Zn_S^0	1	1.11	3.6
Ge_S^-	1/2	0.838	7.02
Ti_S^0	0	1.843	4.33
Li_S^0	1/2	0.764	3.8

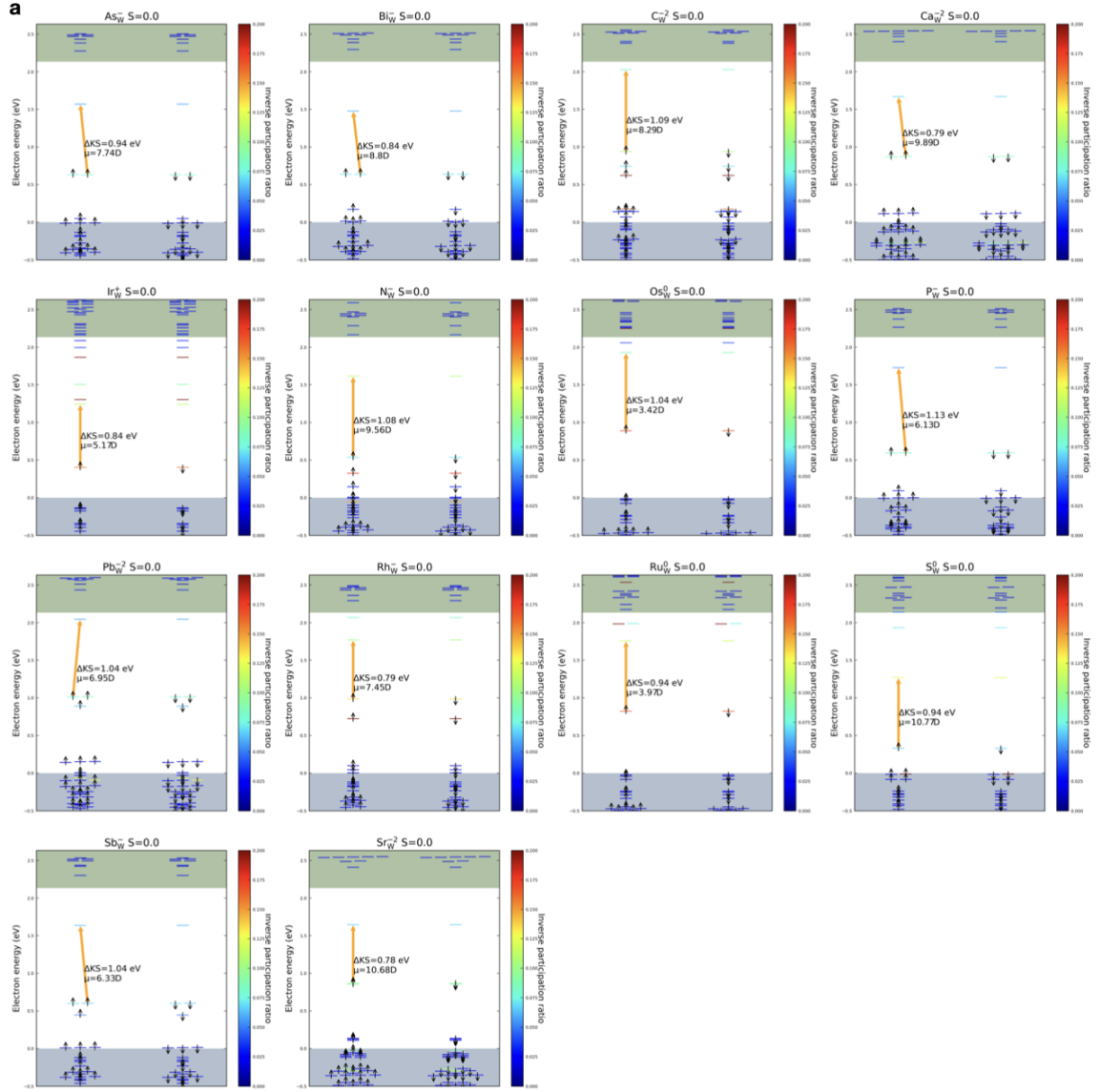
Supplementary Table 1: All the thermodynamically stable two-level defect candidates that show transition dipole moment (TDM) larger than 2.5 D and Kohn-Sham energy difference (Δ KS) larger than 750 meV are summarized in the table below. The Δ KS is computed at single-shot PBE0 level using an α of 0.07, as detailed in the main text.

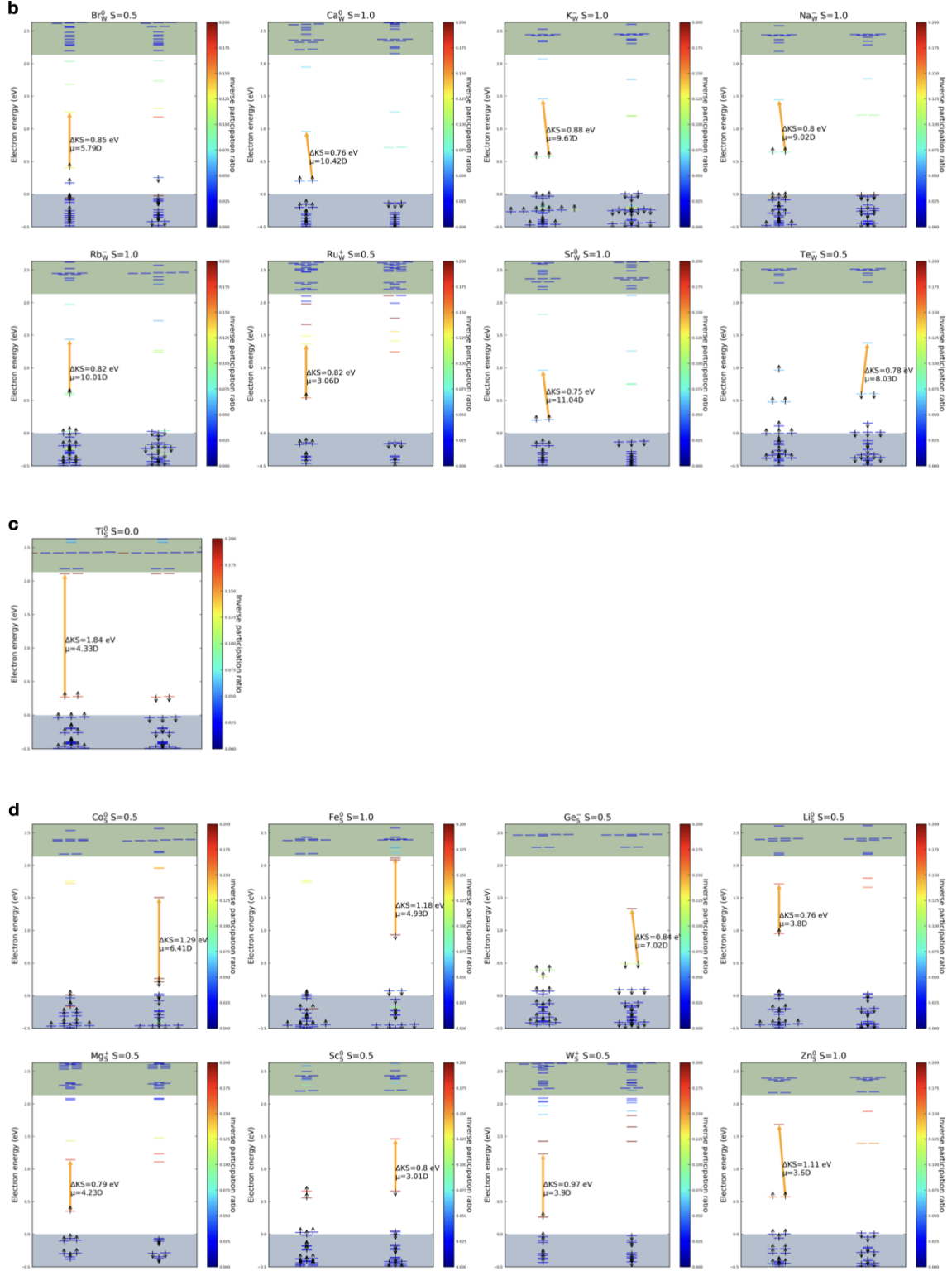
Effect of spin-orbit coupling (SOC) on Co_S defect levels:

	occupation	no SOC	SOC
$d_{x^2-y^2}$	0	-4.06	-4.06
d_{z^2}	1	-5.42	-5.40
$d_{xy} + d_{xz}$	1	-5.56	-5.53

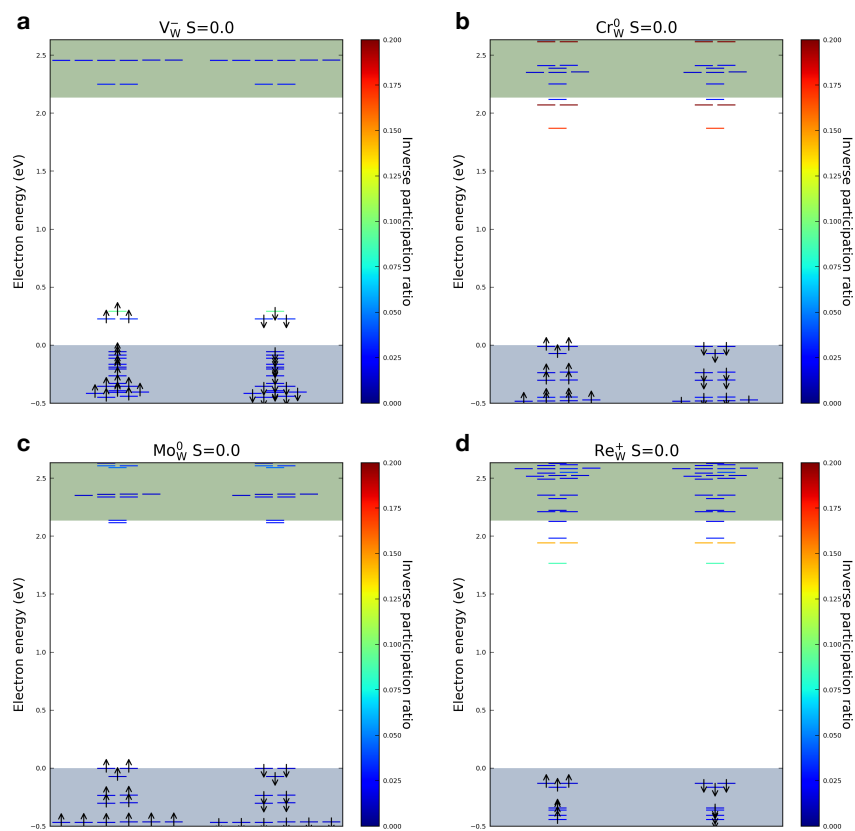
Supplementary Table 2: Eigenvalues (in eV) of defect levels associated with the Co-3d states for the neutral Co_S^0 defect calculated within collinear (no SOC) and noncollinear spin-polarizations (with SOC). All energies are referred to the vacuum level.

Supplementary Fig. 1: In this work, we considered 57 elements for constructing a quantum defect database in WS₂. Our selection covers the majority of the elements, excluding the rare-earth elements and noble gases. The elements that were not considered are colored in gray.

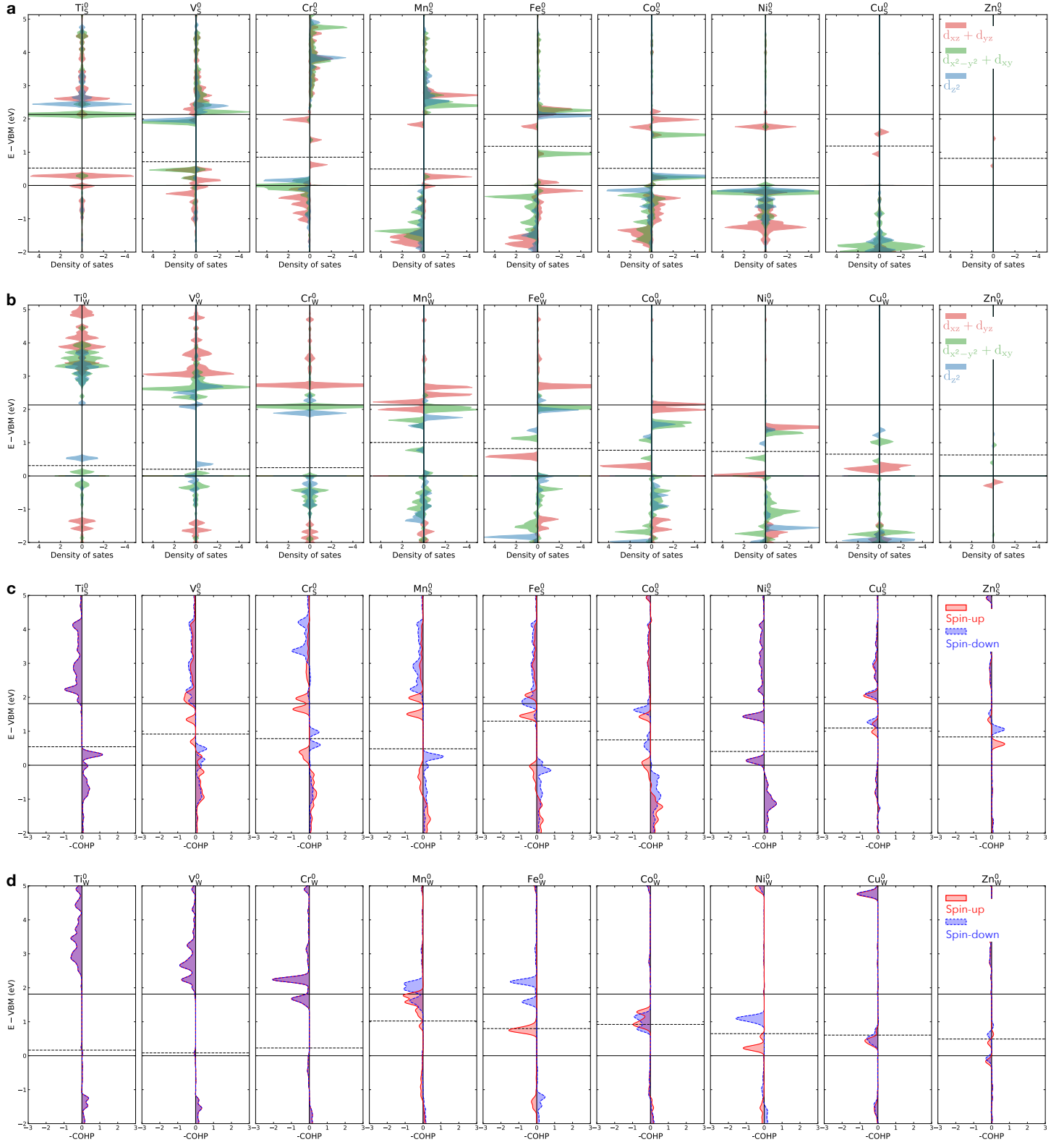




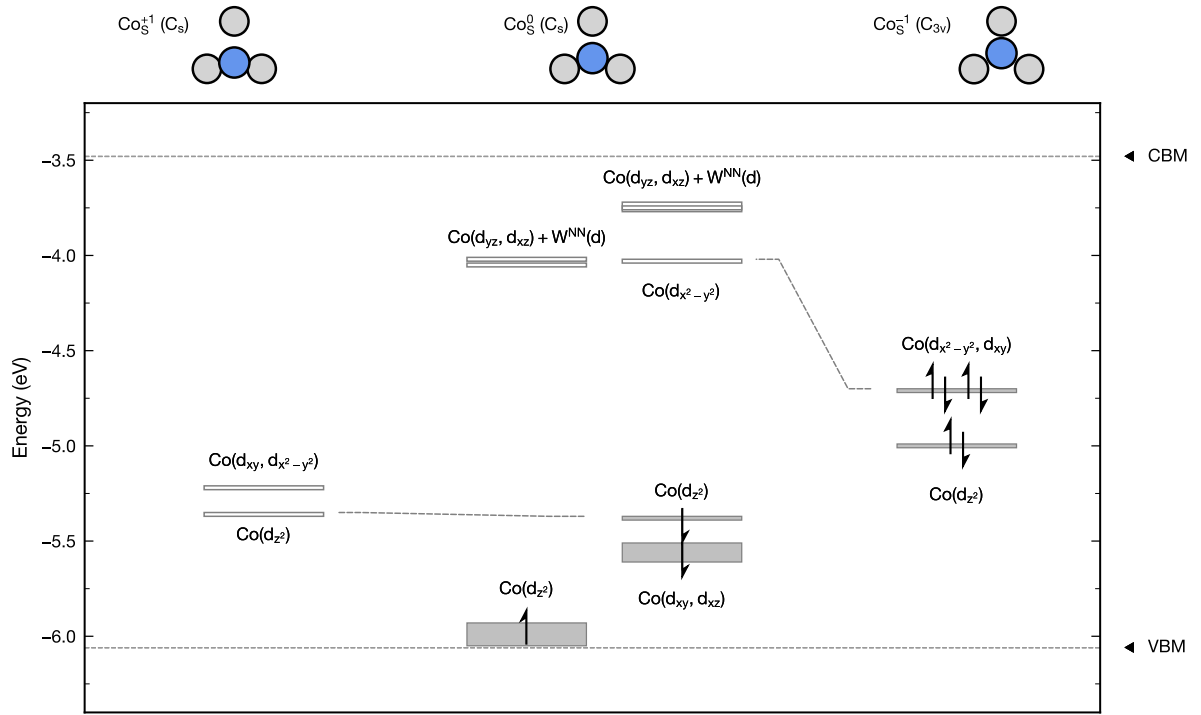
Supplementary Fig. 2: The single-shot PBE0 single-particle defect level diagrams of the screened candidates that have $\Delta KS > 750$ meV and TDM larger than 2.5 D. The two levels that are involved in the transition are highlighted using the arrows, and the localization IPR represented by the color bar. These candidates are grouped into: **a** M_W defects with singlet ground states, **b** M_W defects with nonsinglet ground states, **c** M_S defects with singlet ground states, and **d** M_S defects with nonsinglet ground states.



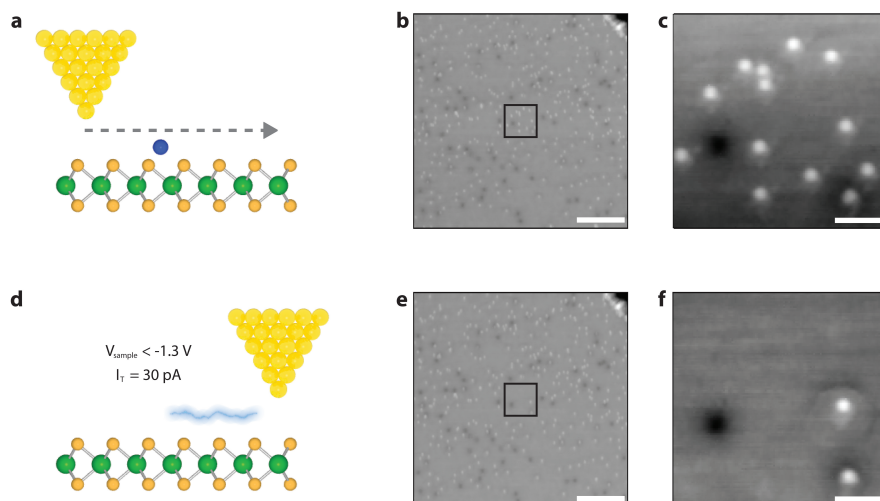
Supplementary Fig. 3: Single-shot PBE0 defect level diagrams of **a** V_W^- , **b** Cr_W^0 , **c** Mo_W^0 , and **d** Re_W^+ in monolayer WS_2 .



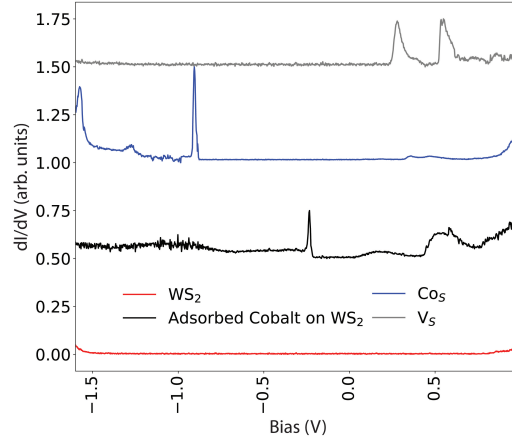
Supplementary Fig. 4: **Partial density of states and crystal orbital Hamilton population (COHP) analysis of 3d transition metal defects in WS_2 .** Projected density of states of the transition metals for **a** substitution on S and **b** substitution on W. The shown density of states are computed at single-shot PBE0 level. The COHP of 3d defects substitution on **a** S and **b** W are evaluated using PBE wave functions. The Fermi level is shown with a dashed horizontal line and band edges are shown with solid horizontal lines.



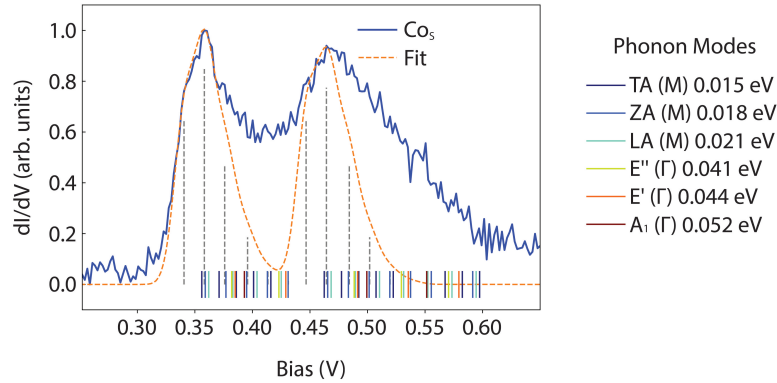
Supplementary Fig. 5: **CoS defect energy levels**. Localized defect states are shown in the +1, 0, and -1 charge states. Resonant states within the valence band and conduction band manifolds are not depicted. The associated single-particle levels are indicated by the horizontal bars (closed for occupied and open for unoccupied states). The dashed lines connect the active orbitals responsible for charging/discharging between two charge states. The band-edge positions indicated in the plot refer to the ones for the pristine WS₂, which are obtained from PBE0 calculations by admixing 22% of Fock exchange. SOC is only applied to the band edges.



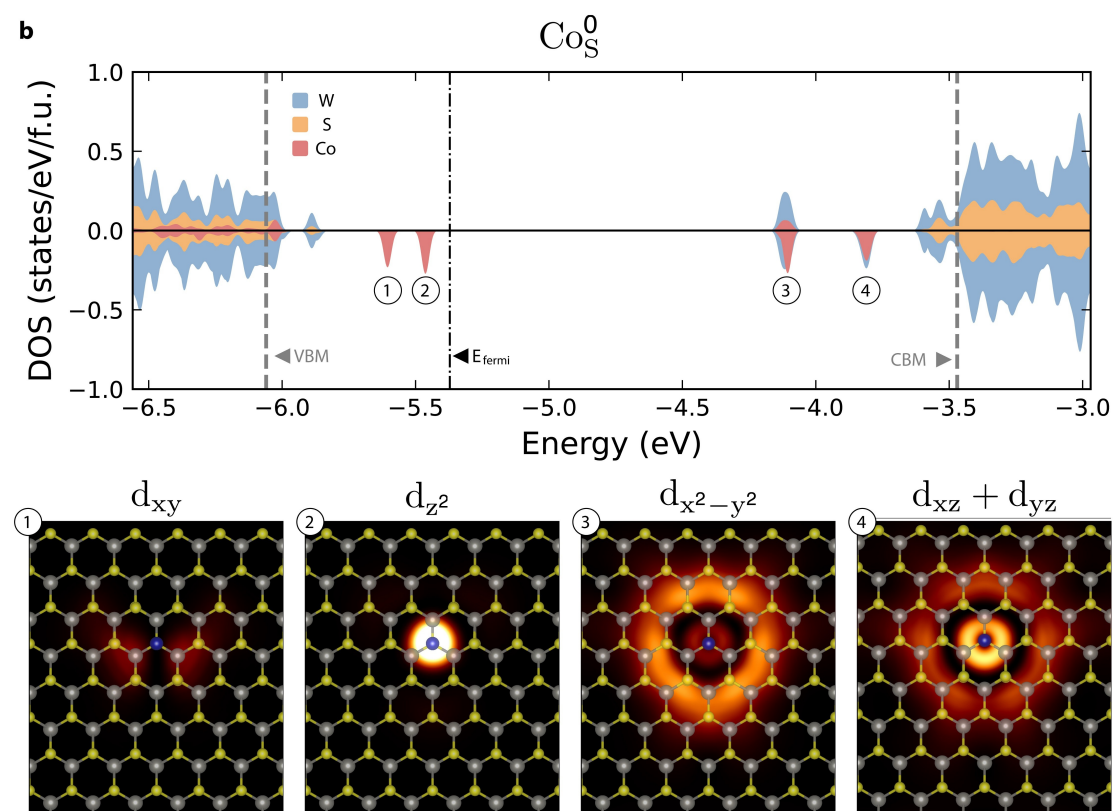
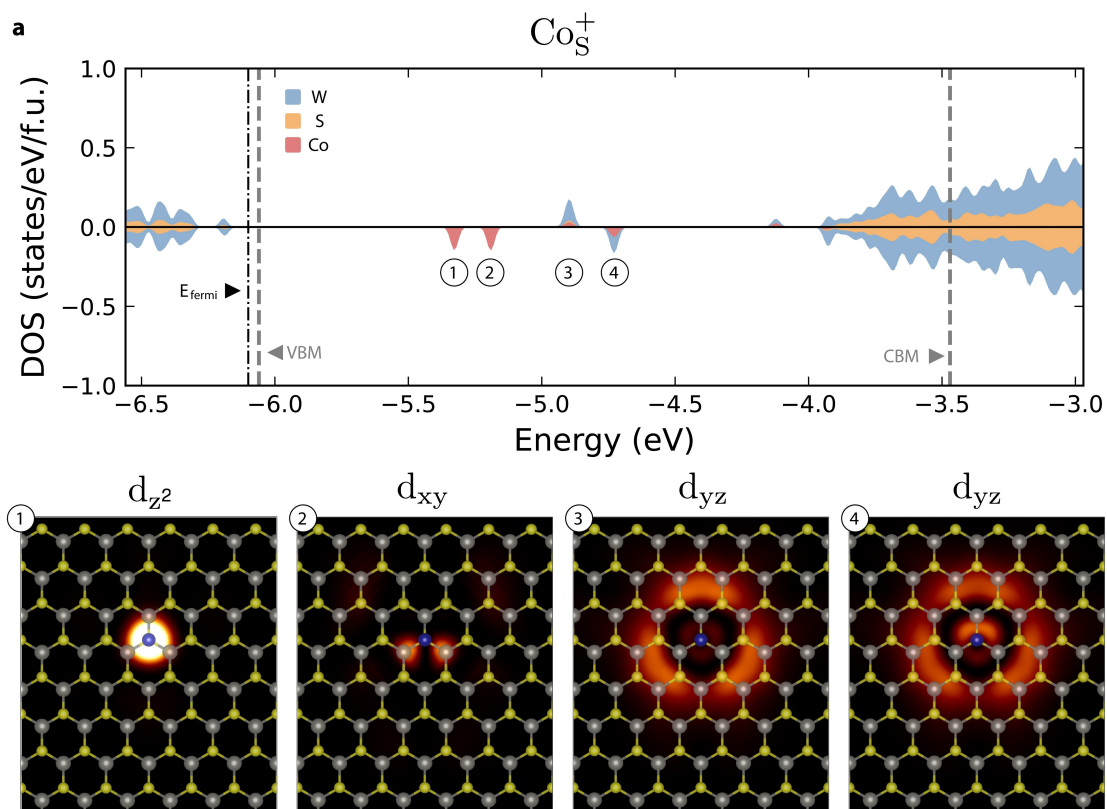
Supplementary Fig. 6: **Tip-induced evaporation/diffusion.** **a** An atomically sharp tip is rastered across a adsorbed Co defect site. **b, c** Scanning tunneling micrographs depicting pristine WS₂ with submonolayer Co atoms adsorbed before local diffusion/evaporation events ($I_{tunnel} = 30$ pA, $V_{sample} = 1.2$ V). Scale bars, 20 nm and 3 nm, respectively. **d** After scanning the local region in **c** at excitation voltage of -1.4 V, the majority of atoms are evaporated (or diffused to a defect capable of absorption (i.e., V_S)). **e, f** Scanning tunneling images of the same large-scale and excited region, where the majority of Co atoms remain that have not been exposed to tunneling-induced motion ($I_{tunnel} = 30$ pA, $V_{sample} = 1.2$ V). Scale bars, 20 nm and 3 nm. Predicted stable sites of adsorbed Co before tip-induced excitation include above a W site, S site, and a hollow site, where any remaining Co adatoms, after a tip-induced event, are expected to remain in a more stable W site^{3,4}.

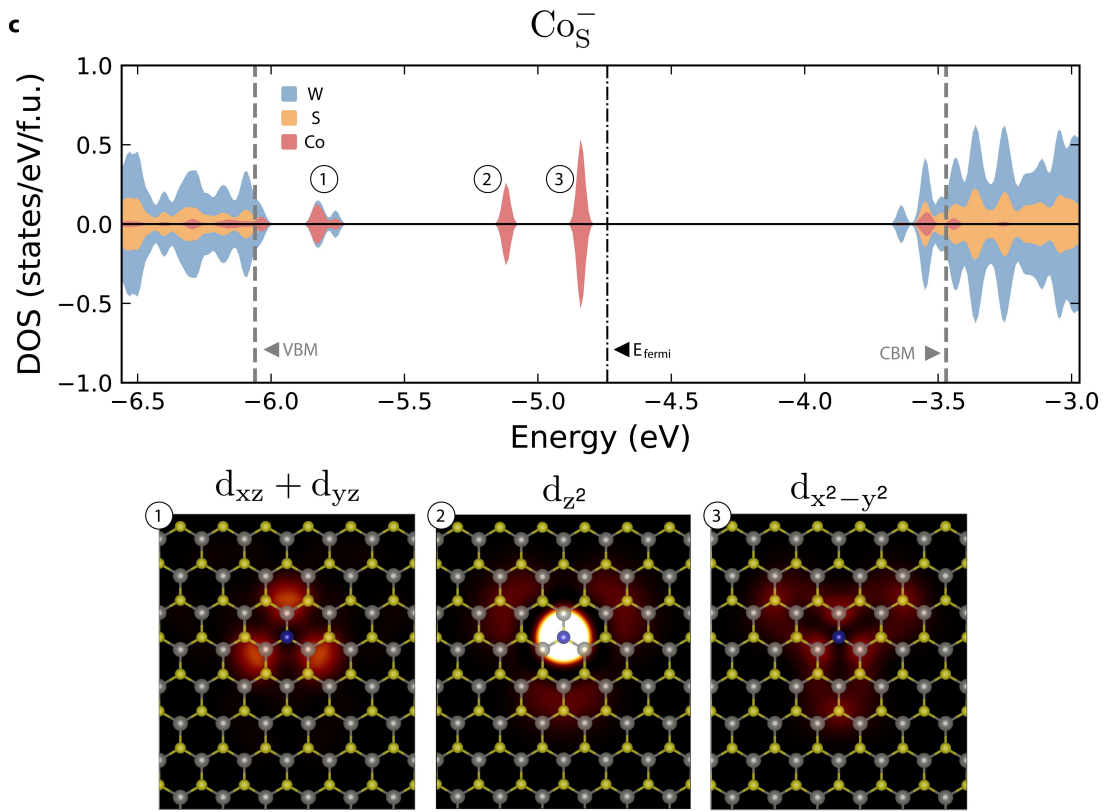


Supplementary Fig. 7: **Point STS Comparison.** dI/dV spectra recorded on as-grown WS_2 (red), adsorbed Co atop WS_2 (black), the CoS defect (blue), and a typical V_S (gray) are presented above ($V_{modulation} = 5$ mV). The as-measured energy gap of an adsorbed Co is 0.97 ± 0.27 eV and 2.0 ± 0.05 eV for CoS . Both WS_2 and V_S recorded energy gaps and point spectra match values that have been reported in the literature⁵.

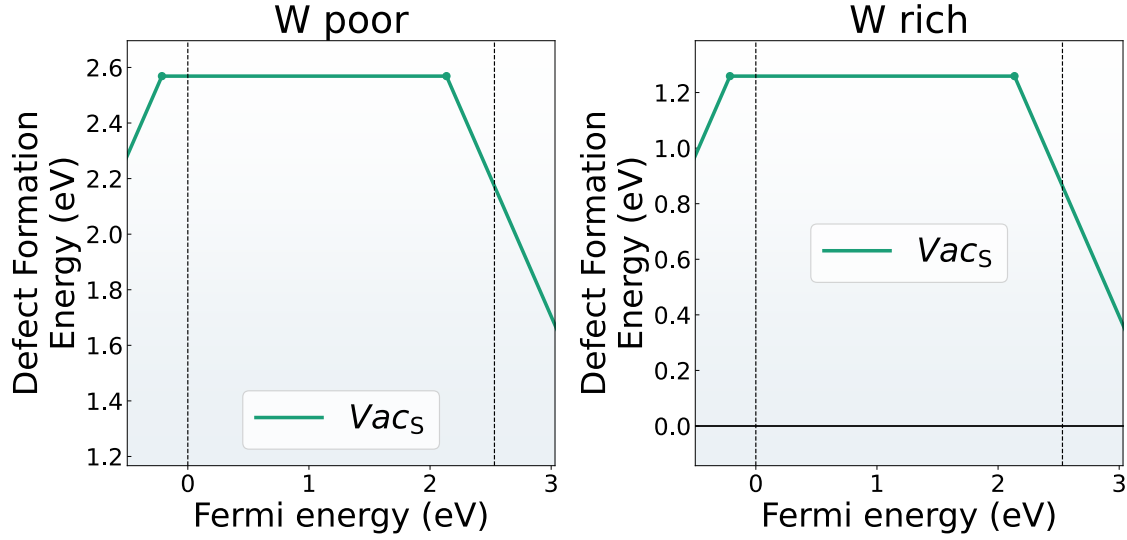


Supplementary Fig. 8: **Phonon Excitation Comparison.** The first and second peaks ($\hbar\omega_{eg}$) within acquired dI/dV are fitted according to the single-mode Franck-Condon model at both 0.36 eV and 0.47 eV. This can be fit as $\frac{dI}{dV}(V) = A \sum_{n=0}^{\infty} e^{-S} \frac{S^n}{n!} \delta(eV - \hbar\omega_{eg} - n\hbar\omega_0)$, where A is an arbitrary scaling factor, S is the Huang-Rhys factor, $\hbar\omega_{eg}$ is the electronic excitation energy or zero-phonon line, and $\hbar\omega_0$ is the excited phonon mode. We use a Gaussian function with a full width at half maximum (Γ) to replace the δ function and account for broadening. Phonon modes were taken from literature values^{6,7}. A Huang-Rhys factor of $S = 1.3$, a first excitation of $\hbar\omega_{eg} = 0.341$ eV, a phonon mode of $\hbar\omega_0 = 0.018$ eV, and a broadening of $\Gamma = 0.021$ eV is estimated for the lower energy defect state, and $S = 1.2$, a first excitation of $\hbar\omega_{eg} = 0.447$ eV, $\hbar\omega_0 = 0.018$ eV, and $\Gamma = 0.021$ eV is estimated for the next available unoccupied state with higher energy.

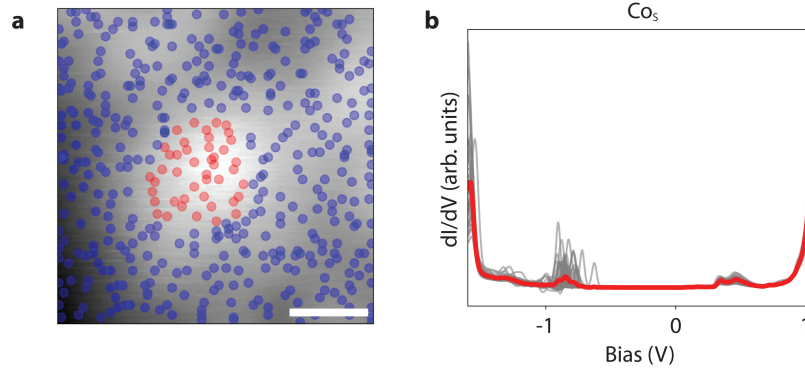




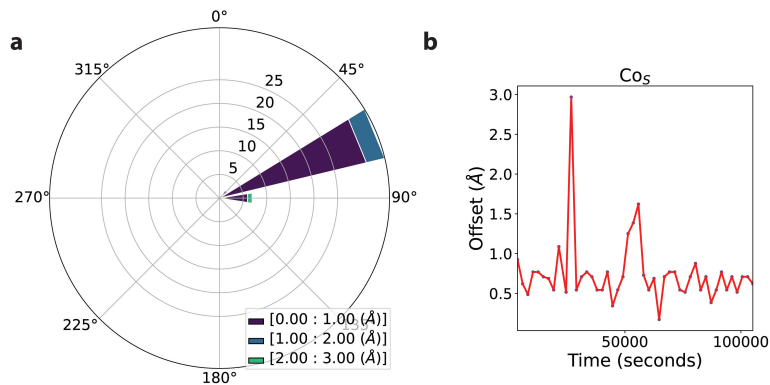
Supplementary Fig. 9: **Element-resolved density of states (DOS) of CoS in WS_2 .** We considered **a** +1, **b** neutral, and **c** -1 charge states. The Scanning Tunneling Spectroscopy results are simulated using PBE0 charge density and energy levels. Wavefunctions of atomic orbitals of Co that contribute most to each Co-related in-gap state are shown below the DOS.



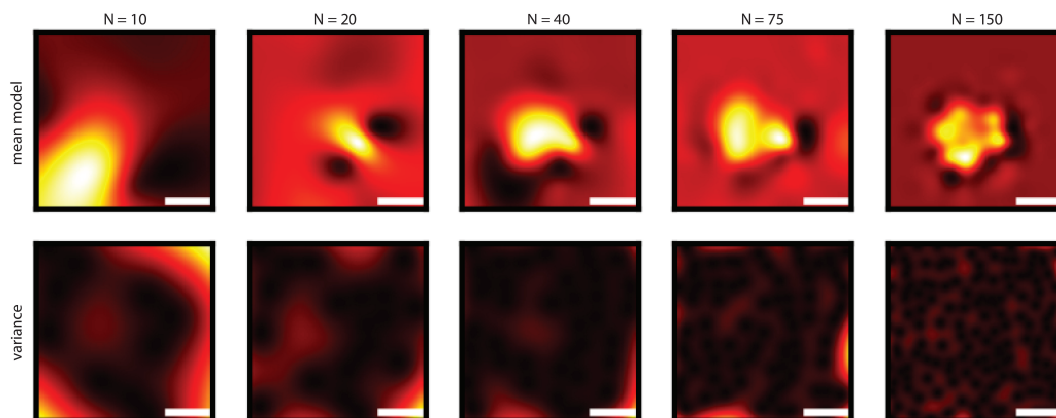
Supplementary Fig. 10: **Thermodynamic charge transition levels of S vacancy in WS_2 .** The defect formation energies are evaluated under W-rich conditions ($\mu_S = -6.25$ eV, $\mu_W = -13.83$ eV) and W-poor conditions ($\mu_S = -4.94$ eV, $\mu_W = 16.45$ eV). The 0/−1 charge transition level is at 2.14 eV with respect to VBM. The vertical dotted lines indicate the band edges.



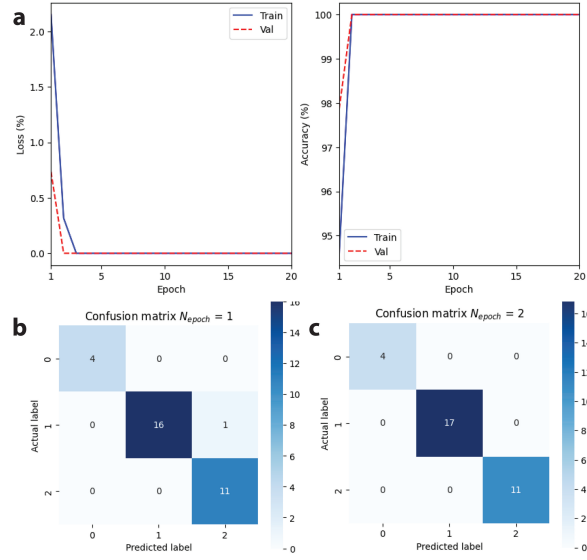
Supplementary Fig. 11: **Hyperspectral Data Collection.** **a** Co_S is identifiable by point bias spectroscopy followed by classification using a trained 1D-CNN, where image tracking can be performed on the defect of interest during an autonomous STS experiment. Outside spectra (either pristine WS_2 or V_S) are bucketed under a different classification (shown in blue). Acquired point STS locations are overlaid on acquired topography ($I_{tunnel} = 30$ pA, $V_{sample} = 1.2$ V). Scale bar, 0.5 nm. **b** Accumulated spectra over Co_S are shown with the mean spectrum that is colored by classification, where a charging peak is measured at -0.84 ± 0.06 eV.



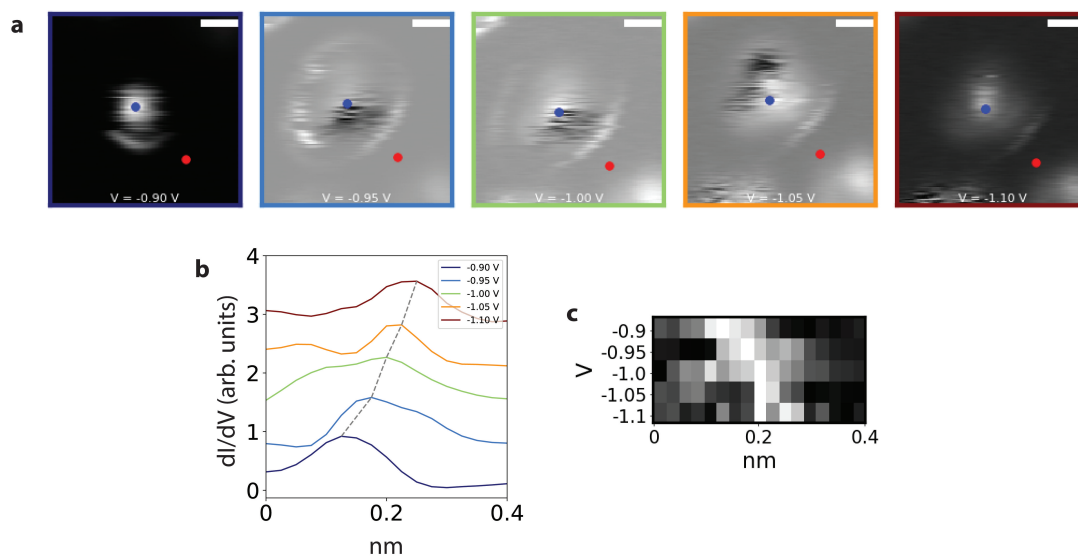
Supplementary Fig. 12: **Drift Correction.** Computed offsets during a CoS autonomous experiment is shown **a** in two dimensions and **b** the magnitude of the 2D vector as a function of time. Drift is multi-directional, but primarily near 70° . In order to correct for drift at each point, a drift rate was calculated between acquired images ($\text{\AA}/\text{s}$) at every interval, and subsequently applied to each timestamped spectra.



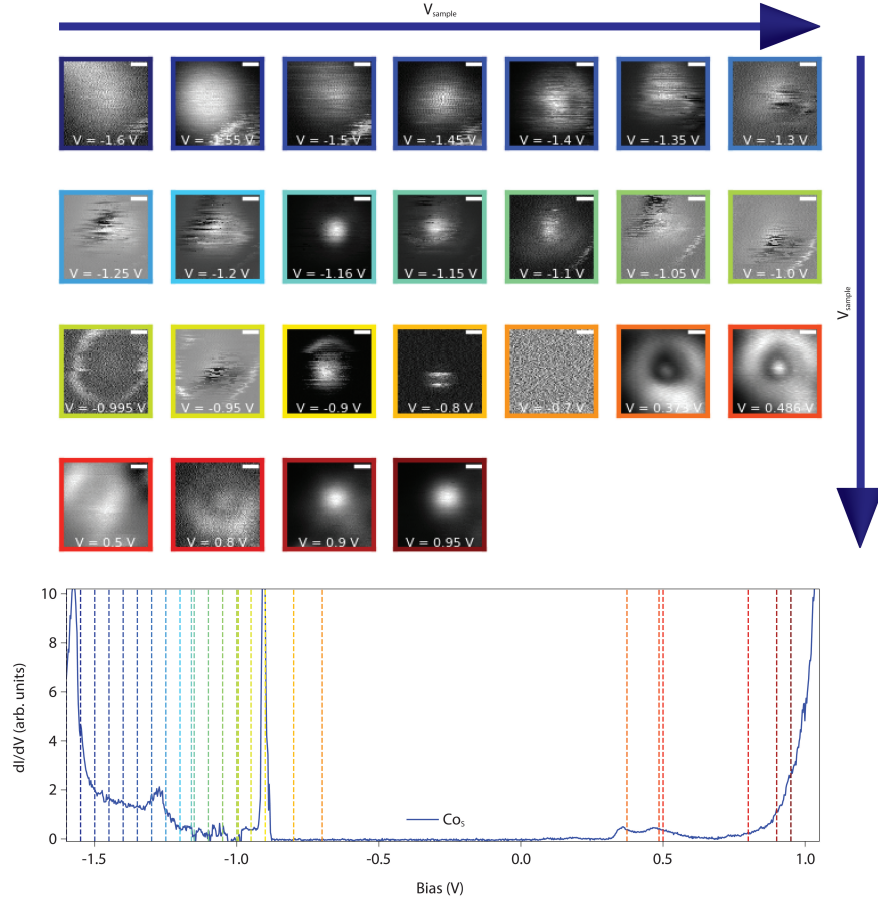
Supplementary Fig. 13: **Autonomous Experimentation.** A live experimental run within a range of 0.25 V to 0.65 V, which is chosen to highlight in-gap states for CoS below the conduction band and above E_F . Scale bars, 0.5 nm. Both the mean model function and variance function are shown at a given interval (N) as the experiment progresses in exploration mode.



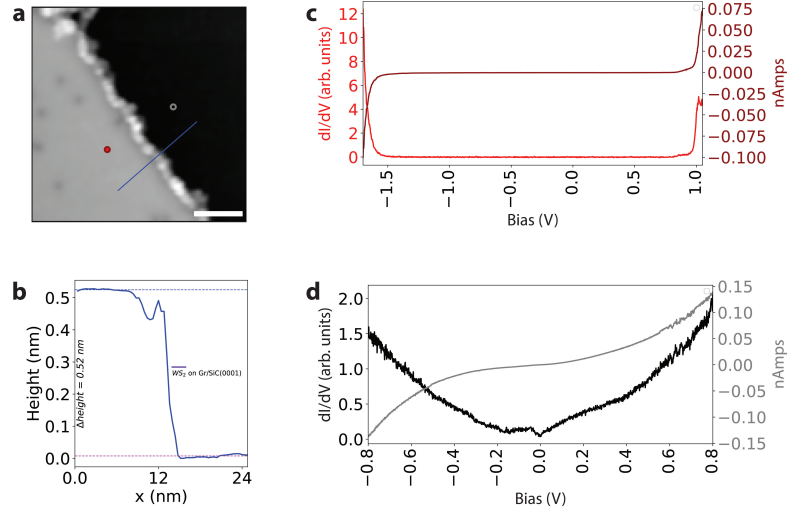
Supplementary Fig. 14: **1D Convolutional Neural Network Performance.** a) Accuracy and loss after 20 training epochs is shown on both training and validation datasets. b) Confusion matrices taken after classification on test data using the argmax value across class probabilities (yielded by the softmax). Training can be concluded after 2 epochs, where test data shows zero off-diagonal elements, loss is minimized, and accuracy is optimized.



Supplementary Fig. 15: **CoS Charging Region.** **a** High resolution scanning tunneling differential conductance maps at -0.90 eV, -0.95 eV, -1.00 eV, -1.05 eV, and -1.10 eV ($V_{\text{modulation}} = 5$ meV). Scale bars, 0.5 nm. Solving for the local maxima at the center of CoS and taking a same-size line scan from the center position to outside the charging region highlights the energetic shift as the bias is ramped to more negative values (shown spatially). Outside the ring, WS₂ remains neutral and, inside the ring, CoS is negatively charged at a given bias. **b** This is shown further as a compilation of linescans and a **c** compiled image as a function of distance and centered along the charging ring.



Supplementary Fig. 16: **Differential Conductance Mapping.** dI/dV images ($V_{\text{modulation}} = 5$ meV) over the point STS ($V_{\text{modulation}} = 5$ meV) region shown for a Co_s defect using a jet color scale, where the energy is ramped from near the VBM of WS_2 to -0.7 eV, from unoccupied peaks of interest, and then to below the CBM of WS_2 . Scale bars, 0.25 nm. Orbitals of the as-formed Co_s and surrounding V_S are visualized as a function of bias voltage. Charging effects are only present in negative sample bias regimes.



Supplementary Fig. 17: **Monolayer WS₂ Identification.** **a** Scanning tunneling image over a WS₂ monolayer edge resting on a graphene/SiC(0001) substrate ($I_{\text{tunnel}} = 30$ pA, $V_{\text{sample}} = 1.2$ V). Scale bar, 10 nm. **b** A height profile taken across the blue line depicted in **a**, where a height difference of ~ 0.5 nm is measured. Regions are further verified with scanning tunneling spectroscopy over both **c** as-grown WS₂ (red circle in **a**) and **d** the graphene/SiC substrate (gray circle in **a**) ($V_{\text{modulation}} = 5$ mV, $I_{\text{set}} = 150$ pA). A band gap of 2.5 eV is measured for as-grown WS₂, and graphene exhibits expected canonical band structure.

SUPPLEMENTARY REFERENCES

- [1] Thomas, J. C. et al. Autonomous scanning probe microscopy investigations over WS₂ and Au{111}. *npj Comput. Mater.* **8**, 99 (2022).
- [2] Kingma, D. P. & Ba, J. Adam: A method for stochastic optimization. Preprint available at <https://arxiv.org/abs/1412.6980> (2014).
- [3] Majd, Z. G., Taghizadeh, S. F., Amiri, P., & Vaseghi, B. Half-metallic properties of transition metals adsorbed on WS₂ monolayer: A first-principles study. *J. Magn. Magn. Mater.* **481**, 129 (2019).
- [4] Xu, W. Electronic structures and magnetic properties of co-adsorbed monolayer WS₂. *J. Mater. Sci. Chem. Eng.* **4**, 32 (2016).
- [5] Schuler, B. et al. Large spin-orbit splitting of deep in-gap defect states of engineered sulfur vacancies in monolayer WS₂. *Phys. Rev. Lett.* **123**, 076801 (2019).
- [6] Molina-Sánchez, A. & Wirtz, L. Phonons in single-layer and few-layer MoS₂ and WS₂. *Phys. Rev. B* **84**, 155413 (2011).
- [7] Molas, M. R., Nogajewski, K., Potemski, M., & Babiński, A. Raman scattering excitation spectroscopy of monolayer WS₂. *Sci. Rep.* **7**, 5036 (2017).